

Electromagnetically induced transparency at a chiral exceptional point

Changqing Wang^{1,7}, Xuefeng Jiang^{1,7}, Guangming Zhao¹, Mengzhen Zhang^{2,3}, Chia Wei Hsu^{0,2,3,4}, Bo Peng^{1,6}, A. Douglas Stone^{2,3}, Liang Jiang^{0,2,3,5} and Lan Yang^{0,1*}

Electromagnetically induced transparency, as a quantum interference effect to eliminate optical absorption in an opaque medium, has found extensive applications in slow-light generation, optical storage, frequency conversion, optical quantum memory and enhanced nonlinear interactions at the few-photon level in all kinds of systems. Recently, there has been great interest in exceptional points, a type of spectral singularity that could be reached by tuning various parameters in open systems, to render unusual features to the physical systems, such as optical states with chirality. Here we theoretically and experimentally study transparency and absorption modulated by chiral optical states at exceptional points in an indirectly coupled resonator system. By tuning one resonator to an exceptional point, transparency or absorption occurs depending on the chirality of the eigenstate. Our results demonstrate a new strategy to manipulate the light flow and the spectra of a photonic resonator system by exploiting a discrete optical state associated with a specific chirality at an exceptional point as a unique control bit. Such an approach is compatible with the state control utilized in quantum gate operation and may open up new avenues for controlling slow light using optical states for optical quantum memory and computing.

riginating from the destructive interference between quantum excitation pathways, electromagnetically induced transparency (EIT) is a notable phenomenon in the optical response of a dielectric medium¹. The transmission spectrum of a probe light is marked by a narrow transparency window in a broad absorption profile, leading to a sharp phase change and a large group delay within the narrow window accompanied by a reduced group velocity of light. EIT and its classical analogues have been demonstrated in gas-phase atomic²⁻⁶, metamaterial/metasurface^{7,8}, plasmonic9-12, optical13-15, optomechanical16-18 and superconducting systems^{19,20}. Among them, all-optical analogues of EIT realized in optical resonant systems, such as metamaterial, plasmonic, photonic crystal and whispering-gallery-mode (WGM) resonators, allow for on-chip and room-temperature operation. Furthermore, the intermodal coupling makes the systems free from the strong control light. However, tuning of EIT via engineering resonant frequencies, coupling strengths and phase delays relies on the external control of continuous parameters such as temperature and optical power, which not only deteriorates fully integrated design, but also brings additional noise and instability due to, for example, thermal fluctuation and non-equilibrium in thermodynamic processes.

Quantum and classical state controls of optical properties have found practical applications in photonic communication and computation, such as qubit logic gates^{21,22}, optical bit storage²³, slow light²⁴ and so on. As the manipulation of optical states has become increasingly practical with the fast-growing cavity-engineering techniques, including field backscattering²⁵, index/material modulation²⁶ and geometry deformation²⁷, it is possible to directly manipulate the resonance spectrum—the discrete quasi-normal modes of the system—to fulfil the demanding conditions of EIT. Up to now, those advantages of optical states have not been utilized to control all-optical EIT, due to the lack of an explicit physical

scheme that could build a connection between the manipulation of optical states and EIT.

Our result brings revenue to this issue by building on the recent progress in non-Hermitian optics. Non-Hermitian wave equations for open systems yielding complex energy spectra with non-orthogonality of eigenstates (quasi-normal modes or resonances) have been utilized to engineer unconventional optical behaviour and functionality^{28,29}. Exceptional points (EPs), a type of degeneracy of the complex spectrum, at which two eigenstates coalescence³⁰, have enabled unconventional effects, including unidirectional reflection/ invisibility³¹, chirality²⁵, enhanced sensitivity^{32,33}, topological optical switching^{34,35} and so on, and been applied to engineering light transport, improved sensing and microlasing^{26,36}. In particular, switching between absorbing and lasing/scattering optical modes has been realized with the assistance of gain/loss^{37,38}. In WGM microresonators, EPs can be reached either by tuning gain-loss contrast and intermodal coupling strength in coupled resonators^{39,40}, or by precisely manipulating the backscattering/refractive index distribution in one resonator^{25,26}. In particular, tuning a WGM resonator to an EP breaks the chiral symmetry of clockwise (CW) and counterclockwise (CCW) light propagation. The single merged eigenstate at the EP can be characterized by its chirality, the ratio of the light circulating in the CW and CCW directions normalized to vary between [-1, 1] (ref. 25). The chirality at EPs is -1 for CCW eigenstates, and 1 for CW eigenstates, which can naturally act as a control bit.

Here we show, both theoretically and experimentally, a way to control optical analogues of EIT in a system of two indirectly coupled WGM microresonators, by directly constructing chiral optical states with the help of EPs. We consider a system as shown in Fig. 1a, where two WGM microresonators μR_1 and μR_2 are coupled to a waveguide with coupling strengths $\gamma_{1,1}$ and $\gamma_{1,2}$, respectively. Resonator μR_1 (μR_2) supports WGMs with the resonant frequency

¹Department of Electrical and Systems Engineering, Washington University, St Louis, MO, USA. ²Departments of Applied Physics and Physics, Yale University, New Haven, CT, USA. ³Yale Quantum Institute, Yale University, New Haven, CT, USA. ⁴Ming Hsieh Department of Electrical and Computer Engineering, University of Southern California, Los Angeles, CA, USA. ⁵Pritzker School of Molecular Engineering, University of Chicago, Chicago, IL, USA. ⁶Present address: Globalfoundries, East Fishkill, NY, USA. ⁷These authors contributed equally: Changqing Wang, Xuefeng Jiang. *e-mail: yang@seas.wustl.edu

ARTICLES NATURE PHYSICS

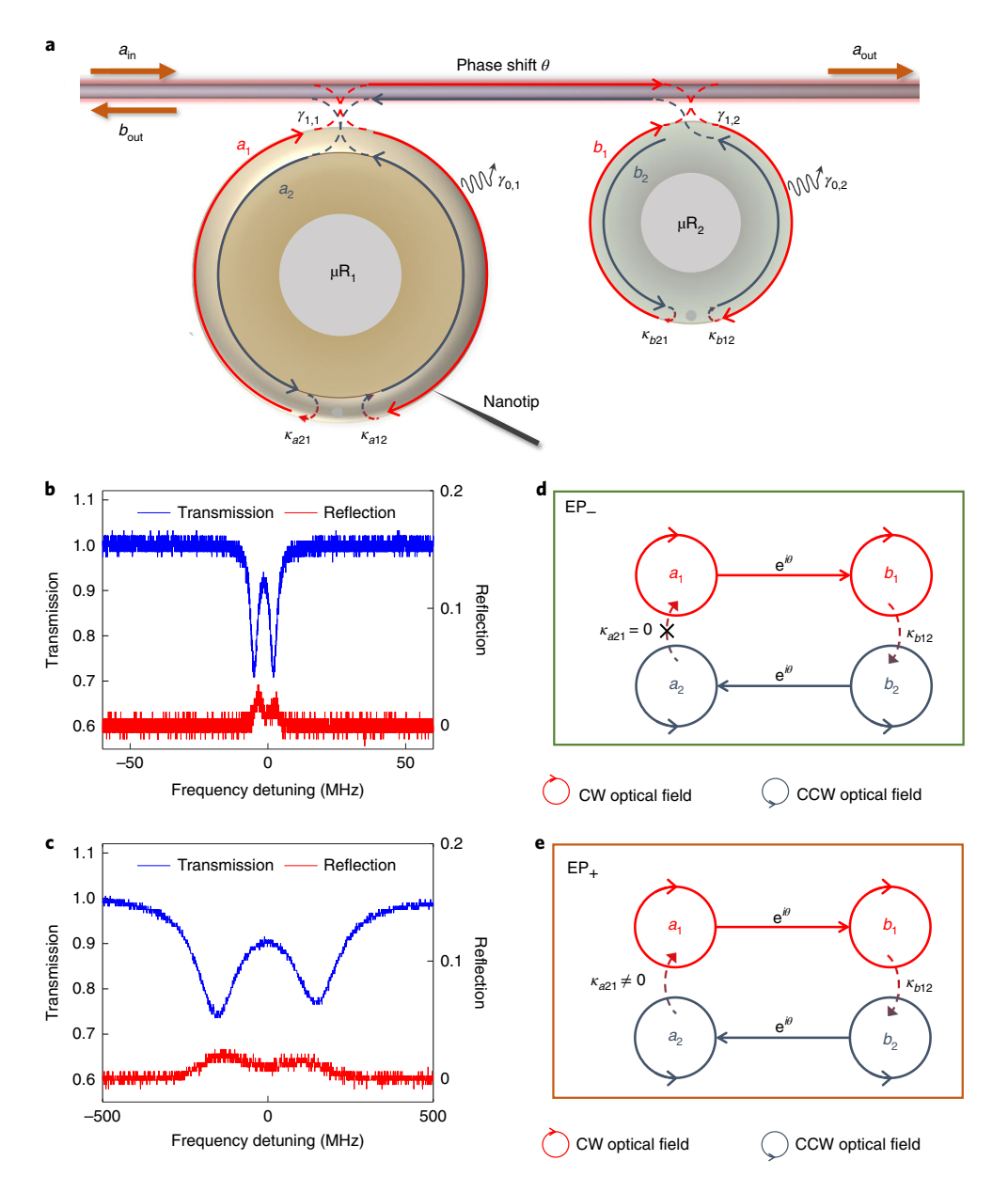


Fig. 1 Indirectly coupled WGM microresonators with manipulation of chirality. **a**, A schematic diagram of the system consisting of indirectly coupled WGM microresonators. A microtoroid and a microdisk are coupled to a fibre taper with coupling strengths $\gamma_{1,1}$ and $\gamma_{1,2}$, respectively. They both support CW and CCW modes ($a_{1,2}$ and $b_{1,2}$) that have intrinsic loss ($\gamma_{0,1}$ and $\gamma_{0,2}$). Intrinsic perturbations on the surfaces of each resonator can be modelled as an effective scatterer marked by a grey dot, which induces coupling between CW and CCW modes. A nanotip can be applied to the mode volume of μR₁ to induce asymmetric coupling between the CW and CCW modes and breaks the chiral symmetry of μR₁. An optical path loop is formed: $a_1^{\sqrt{\gamma_{1,1}}}$ dibre mode ($e^{i\theta}$) $\frac{\sqrt{\gamma_{1,2}}}{\sqrt{\gamma_{1,1}}}$ applies the mode ($e^{i\theta}$) $\frac{\sqrt{\gamma_{1,1}}}{\sqrt{\gamma_{1,1}}}$ applies $a_2^{-\kappa_{0,1}}$ $a_1^{-\kappa_{0,1}}$ $a_2^{-\kappa_{0,1}}$ $a_1^{-\kappa_{0,1}}$ $a_2^{-\kappa_{0,1}}$ $a_1^{-\kappa_{0,1}}$ $a_2^{-\kappa_{0,1}}$ $a_1^{-\kappa_{0,1}}$ $a_2^{-\kappa_{0,1}}$ $a_2^{-\kappa$

 $ω_1$ ($ω_2$) and intrinsic loss rate $γ_{0,1}$ ($γ_{0,2}$). The CW and CCW modes are coupled with each other via backscattering on the resonator surfaces. In $μR_2$, we assume that the coupling strength of the scattering from CW to CCW ($κ_{b12}$) is identical to that from CCW to CW ($κ_{b21}$). In $μR_1$, asymmetric backscattering can be introduced by additional perturbations; that is, the scattering-induced coupling from CW to CCW ($κ_{a12}$) is not equal to that from CCW to CW ($κ_{a21}$). The dynamics of the system can be described by the coupled mode equations, given by:

$$\frac{\mathrm{d}a_1}{\mathrm{d}t} = -i\omega_1 a_1 - \frac{\gamma_{0,1} + \gamma_{1,1}}{2} a_1 - i\kappa_{a21} a_2 - \sqrt{\gamma_{1,1}} a_{\mathrm{in}}$$
 (1)

$$\frac{\mathrm{d}a_{2}}{\mathrm{d}t} = -i\omega_{1}a_{2} - \frac{\gamma_{0,1} + \gamma_{1,1}}{2}a_{2} - i\kappa_{a12}a_{1} - \mathrm{e}^{i\theta}\sqrt{\gamma_{1,1}\gamma_{1,2}}b_{2}$$
 (2)

$$\frac{\mathrm{d}b_{1}}{\mathrm{d}t} = -i\omega_{2}b_{1} - \frac{\gamma_{0,2} + \gamma_{1,2}}{2}b_{1} - i\kappa_{b21}b_{2} - \sqrt{\gamma_{1,2}}e^{i\theta}\left(a_{\mathrm{in}} + \sqrt{\gamma_{1,1}}a_{1}\right)$$
(3)

NATURE PHYSICS ARTICLES

$$\frac{\mathrm{d}b_2}{\mathrm{d}t} = -i\omega_2 b_2 - \frac{\gamma_{0,2} + \gamma_{1,2}}{2} b_2 - i\kappa_{b12} b_1 \tag{4}$$

where a_1 (b_1) and a_2 (b_2) correspond to the fields of CW and CCW modes in μR_1 (μR_2), respectively. The angle θ is the phase shift accumulated when light propagates in the fibre between the resonators. The output field is given by:

$$a_{\text{out}} = \sqrt{\gamma_{1,2}} b_1 + e^{i\theta} \left(a_{\text{in}} + \sqrt{\gamma_{1,1}} a_1 \right) \tag{5}$$

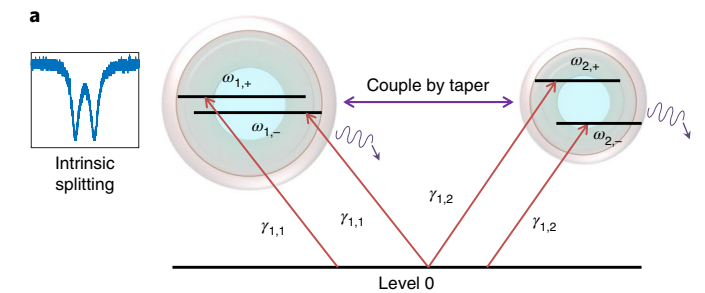
We assume that the resonant frequency detuning between the two resonators is zero; that is, $\Delta_1 = \Delta_2 = \Delta$ (see Supplementary Section C2 for non-zero detuning). Then we obtain the transmission spectrum as:

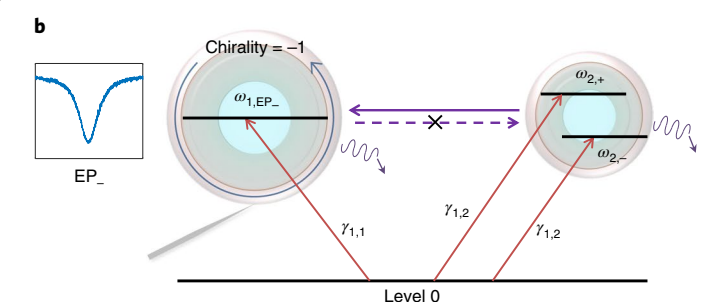
$$T = \frac{\left[-(\gamma_{0,1} - 2i\Delta)^2 + \gamma_{1,1}^2 - 4\kappa_{a21}\kappa_{a12} \right] \left[-(\gamma_{0,2} - 2i\Delta)^2 + \gamma_{1,2}^2 - 4\kappa_{b21}\kappa_{b12} \right]}{P + \left[(\gamma_{0,1} + \gamma_{1,1} - 2i\Delta)^2 + 4\kappa_{a21}\kappa_{a12} \right] \left[(\gamma_{0,2} + \gamma_{1,2} - 2i\Delta)^2 + 4\kappa_{b21}\kappa_{b12} \right]} \right|^2$$
(6)

where $P = 16\gamma_{1,1}\gamma_{1,2}\kappa_{a21}\kappa_{b12}e^{2i\theta}$ plays the critical role of introducing an interference effect in the optical path. We use this theoretical model for numerical simulation in this study (detailed calculations are provided in Supplementary Section A1).

In our experimental set-up, a microtoroid is used as μR_1 and a microdisk as µR₂, which are coupled to a fibre taper waveguide. The two resonators support WGMs in the 1,447 nm wavelength band with similar polarization (see Supplementary Section B for the influence of potential polarization mismatch); the modes in the microtoroid and the microdisk have disparate quality factors (Q) of 6.9×10^7 and 1.6×10^5 , respectively. The system is probed by a frequency-swept laser that is injected into the left port of the fibre taper. Both the transmission and the reflection signals are monitored by photodetectors with the help of an optical switch and two circulators. We first individually characterize the microtoroid (μR_1) and microdisk (µR₂) resonators. In the transmission spectra, the mode splitting is observable for the high-Q modes in the microtoroid (Fig. 1b), indicating that the degeneracy of CW and CCW modes is broken through some intrinsic perturbation (for example, geometry or defect-based). For the low-Q modes in the microdisk, the mode splitting is observable only when weakly coupled to the taper (Fig. 1c), because the broadened linewidth blurs the two dips in the transmission spectrum when the coupling is large. For both resonators, the reflection spectra (Fig. 1b,c) also indicate the existence of backscattering, caused by features such as surface roughness and nanoparticle accumulation.

The optical analogues of EIT in resonator systems originate from cancellation of intracavity fields due to optical destructive interference⁴¹. In particular, a resonant mode is excited not only by the input light field directly, but also by the modal coupling to another resonant mode. These two excitation pathways can destructively interfere with each other and lead to EIT. In our system, light propagation in both forward and backward directions is allowed in the fibre taper between the two resonators, which could be modelled as forward and backward waveguide channels. With the help from these channels and the backscattering in each resonator, a loop is formed in the optical path (Fig. 1a): light from mode a_1 in μR_1 couples to the fibre in the forward direction $(\sqrt{\gamma_{1,1}})$; after propagating in the fibre with the phase modified by the optical path length (e^{iθ}), it couples into mode $b_1\left(\sqrt{\gamma_{1,2}}\right)$ in μR_2 , where the backscattering enables the light to couple to mode b_2 (κ_{b12}); subsequently the light couples to the fibre in the backward direction $(\sqrt{\gamma_{1,2}})$, propagating backwards accumulating phase $(e^{i\theta})$; when the light meets μR_1 , it couples into mode a_2 $(\sqrt{\gamma_{1,1}})$; through





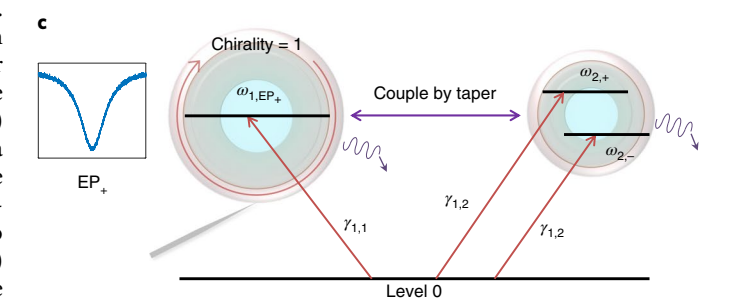


Fig. 2 | Level diagrams of indirectly coupled WGM microresonators.

a, A level diagram of the system when the nanotip is not applied to μR_1 . The degeneracy of each resonator is lifted due to intrinsic perturbations, forming non-chiral standing-wave supermodes. The spectrum of μR_1 shows mode splitting (inset). The levels $\omega_{1\pm}$ and $\omega_{2\pm}$ are eigenfrequencies of μR_1 and μR_2 , respectively, and 0 represents the level at which the optical modes are not excited. **b**, A level diagram of the system when the nanotip steers μR_1 to EP_ with chirality –1 and CCW eigenmode (blue arc with arrow). The spectrum of μR_1 shows a single dip (inset). The coupling between the two resonators breaks due to lack of backscattering from CCW to CW in μR_1 . **c**, A level diagram when the nanotip steers μR_1 to EP_ with chirality 1 and CW eigenmode (red arc with arrow). The spectrum of μR_1 shows a single dip (inset). Due to $\gamma_{1,1} \ll \gamma_{1,2}$, the level structure can be regarded as two sets of Λ-type levels $\{\omega_{1,EP+1},\omega_{2+1},0\}$.

backscattering from CCW to CW, if there is any, the light couples back to mode a_1 (κ_{a21}). The field travelling a round trip in the loop will accumulate a phase shift $\Delta\phi$ that is equal to the phase angle of the coefficient $\gamma_{1,1}\gamma_{1,2}\kappa_{a21}\kappa_{b12}\mathrm{e}^{2i\theta}$. At the same time, mode a_1 is directly excited by the forward-propagating field in the fibre taper. Therefore, optical interference occurs between these two optical paths for the excitation of mode a_1 . In addition, mode b_1 can also be regarded as the starting and ending point of the optical path loop, which indicates that the same type of interference occurs in the excitation of b_1 . As a result, the field intensity in a_1 and b_1 can be enhanced by the constructive interference ($\Delta\phi=\pi$), which can be controlled by the phase angle θ .

To see chiral states of μR_1 on the optical interference, we introduce a nanotip to the vicinity of the microtoroid (Fig. 1a), which

ARTICLES NATURE PHYSICS

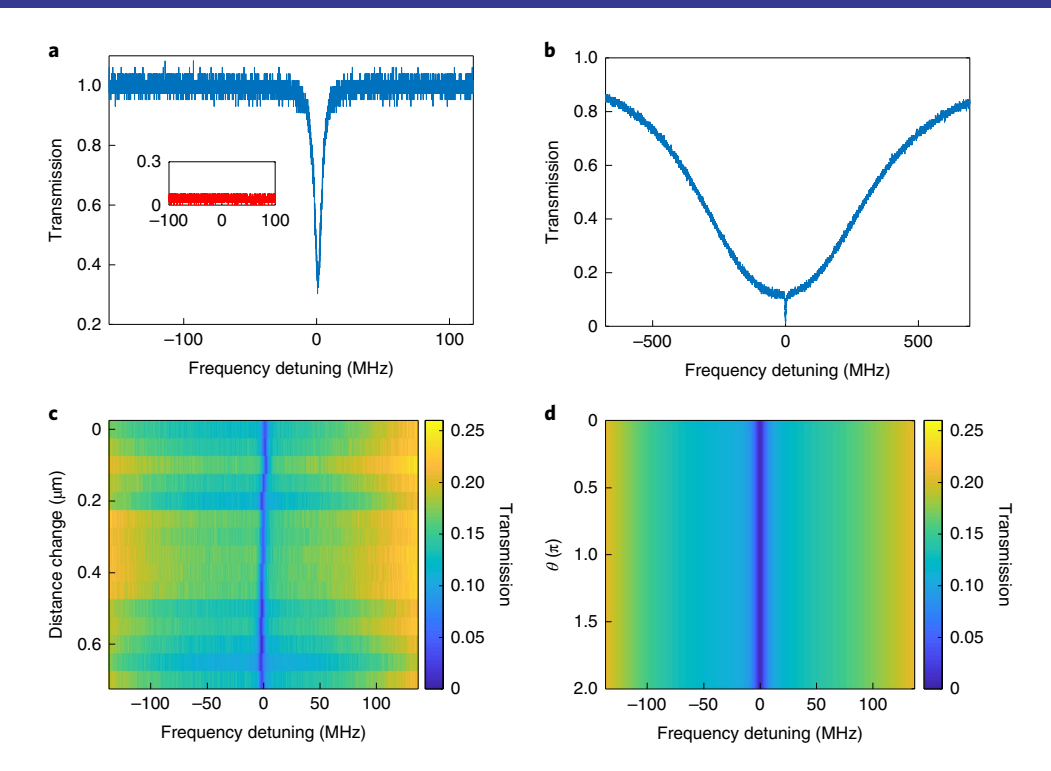


Fig. 3 | Absorption at EP_ with chirality -1. a, The experimentally measured transmission spectrum when characterizing μ R₁ with incident light from the right port. The reflection spectrum is flat zero as shown in the inset. **b**, The experimentally measured transmission spectrum of the system with a randomly picked phase angle θ . **c**, Experimentally measured transmission spectra with the variation of the distance between μ R₁ and μ R₂. μ R₁ is critically coupled to the taper. From top to bottom, the distance is changed by a step of 50 nm. **d**, The numerical simulation result of transmission spectra with the variation of θ . The parameters used in the simulation are obtained by fitting the spectrum in **a**: $\kappa_{a21} = 0$, $\kappa_{a12} = (0.2196 - 0.6974i)$ MHz, $\kappa_{b21} = \kappa_{b12} = (0.1327 - 0.0306i)$ GHz, $\gamma_{0.1} = 5.570$ MHz, $\gamma_{0.1} = 5.570$ MHz, polarization mismatch $\phi = 0.03\pi$.

perturbs the evanescent fields of the modes and their backscattering-induced modal coupling in an asymmetric way^{25,32}. As a result, the backscattering-induced coupling strengths can be expressed as $\kappa_{a12(a21)} = \epsilon_{a1} e^{\pm i2m_a\beta_{a1}} + \epsilon_{a2} e^{\pm i2m_a\beta_{a2}}$ and $\kappa_{b12(b21)} = \epsilon_b e^{\pm i2m_b\beta_b}$, where $\beta_{a1(a2)}$ and β_b are the azimuthal positions of the nanoscatters with perturbations $\epsilon_{a1(a2)}$ and ϵ_b on μR_1 and μR_2 , respectively, and $m_{a(h)}$ is the azimuthal mode number of μR_1 (μR_2) (see Methods and Supplementary Section A3 for detail of the specific theoretical model). The perturbation skews the eigenstates of μR_1 and the resonator can be tuned to an EP with a single merged eigenstate of either chirality 1 or -1 (see Supplementary Section C4 for chirality tuning). We define EP_ and EP_. For EP_, the eigenmode rotates in the CCW direction corresponding to chirality -1. The backscattering from CW to CCW is non-zero, and the backscattering from CCW to CW is zero; that is, $\kappa_{a12} \neq 0$ and $\kappa_{a21} = 0$. For EP₊, the eigenmode rotates in the CW direction (chirality +1). The backscattering from CW to CCW is zero, and the backscattering from CCW to CW is non-zero; that is, $\kappa_{a12} = 0$ and $\kappa_{a21} \neq 0$. In each case, the vanishing of κ_{a12} or κ_{a21} is achieved simply by properly adjusting the radial and azimuthal position of the nanotip near the rim of the microtoroid. At EP_, the coefficient $\gamma_{1,1}\gamma_{1,2}\kappa_{a21}\kappa_{b12}e^{2i\theta}$ becomes zero and thus the optical path loop is broken (Fig. 1d). As a result, the modes in the two resonators do not interfere with each other and are excited by the waveguide mode sequentially. At EP₊, the optical loop path still exists, because $\kappa_{a21} \neq 0$ and hence the coefficient $\gamma_{1,1}\gamma_{1,2}\kappa_{a21}\kappa_{b12}e^{2i\theta}$ does not vanish (Fig. 1e). By proper tuning of the phase angle θ , constructive/destructive loop interference can occur for the excitation of the intracavity fields, which could lead to an absorption or transparency window in the spectrum. Here the transparency (absorption) window is a single narrow peak (dip), as a result of the coalescence of eigenstates at EPs. A general discussion of non-EP configurations is presented in Supplementary Section C1.

To understand the necessary conditions of EIT in this system with EP-controlled chirality, we construct energy-level diagrams based on the eigenfrequencies of the resonator modes. Without perturbation by the nanotip, there are two eigenfrequencies in μR_1 (μR_2) corresponding to level $\omega_{1,\pm}$ $(\omega_{2,\pm})$ that are coupled to level 0 with coupling strength $\gamma_{1,1}$ ($\gamma_{1,2}$), where level 0 represents the level at which the optical modes of resonators are not excited (Fig. 2a). Levels $\omega_{1,\pm}$ and $\omega_{2,\pm}$ are coupled indirectly via the taper. With a nanotip steering μR_1 to the EPs, $\omega_{1,+}$ and $\omega_{1,-}$ will merge and become degenerate. At EP_ with chirality -1, the CCW eigenmode field in μR_1 cannot be scattered back into the CW direction. As a result, the flow can transfer only from level $\omega_{2,\pm}$ to level $\omega_{1,EP-}$ but not in the opposite direction, indicating that these two levels are not coupled (Fig. 2b). On the other hand, at EP₊ with chirality 1, the CCW field can be scattered back into the CW eigenmode, and thus the coupling between levels $\omega_{1,EP+}$ and $\omega_{2,\pm}$ exists (Fig. 2c). If $\gamma_{1,1} \ll \gamma_{1,2}$, we could neglect the coupling between level $\omega_{\scriptscriptstyle 1,EP+}$ and 0, and the system at EP₊ will support two sets of Λ -type levels { $\omega_{1,EP+},\omega_{2,+},0$ } (μ R₂ can also be treated as having one standing wave mode under a certain approximation, see Supplementary Section A4). In our system with highly dissimilar intrinsic loss rates ($\gamma_{0.1} \approx 0.025 \gamma_{0.2}$) for the modes in the two resonators, this condition is not hard to satisfy, as long as we choose $\gamma_{1,1} < 40\gamma_{0,1}$ and keep $\gamma_{1,2}$ in the same order as $\gamma_{0,2}$. Therefore, the level diagram at EP₊ is analogous to the Λ -type energy levels that conventionally lay the foundation for EIT.

On the basis of the level diagram at EP₊, we can further identify the parameter regimes for which the analogue of EIT could be enabled. First, the coupling between level $\omega_{1,\text{EP+}}$ and level $\omega_{2,\pm}$ needs to be strong in analogy to the requirement of a large Rabi frequency of the control laser in the atomic EIT configuration. The effective coupling coefficient between level $\omega_{1,\text{EP+}}$ and level $\omega_{2,\pm}$ is proportional to $\gamma_{1,1}\gamma_{1,2}\kappa_{a21}\kappa_{b12}e^{2i\theta}$ and thus can be elevated not only by

NATURE PHYSICS ARTICLES

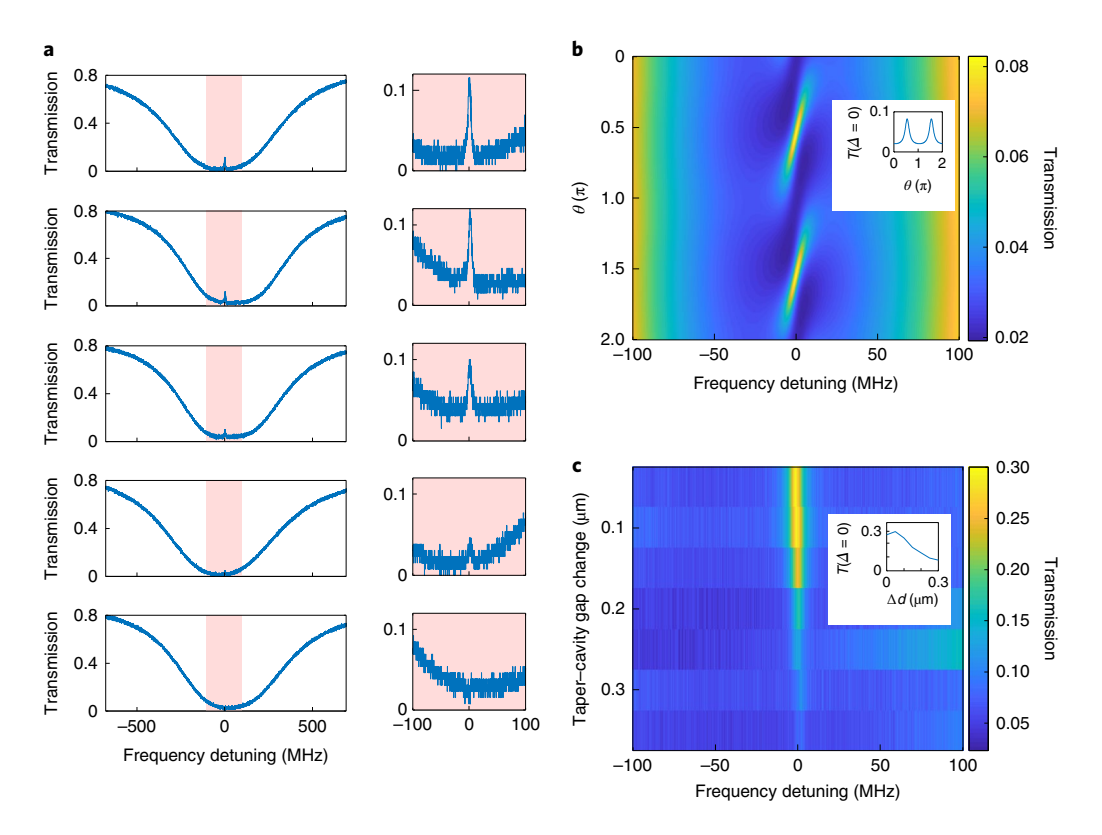


Fig. 4 | Transparency at EP₊ with chirality 1. **a**, Experimentally measured transmission spectra with different phase angles θ . Close-ups of the spectra within the orange-shaded regions are shown in the insets. μ R₂ is almost critically coupled to the taper and μ R₁ is strongly coupled to the taper. **b**, The numerical simulation result of transmission spectra with the variation of θ . The inset shows the transmission at zero detuning ($T(\Delta = 0)$) versus θ . The parameters used in the simulation are obtained by fitting the spectrum in **a**: $\kappa_{a21} = (7.114 - 0.0318i)$ MHz, $\kappa_{a12} = 0$, $\kappa_{b21} = \kappa_{b12} = (0.1337 - 0.0306i)$ GHz, $\gamma_{0,1} = 3.024$ MHz, $\gamma_{1,1} = 11.98$ MHz, polarization mismatch $\phi = 0.03\pi$. **c**, Experimentally measured transmission spectra with the variation of the gap between μ R₁ and the taper. The peak of the transparency window in the transmission spectra is maximized by optimizing the destructive interference with a fixed phase angle θ . From top to bottom, the gap is increased by a step of 50 nm. The inset shows the transmission at zero detuning ($T(\Delta = 0)$) as a function of the change in the taper-cavity gap (Δd).

increasing the coupling coefficients $\gamma_{1,1}$ and $\gamma_{1,2}$, but also by enhancing the intracavity scattering rates κ_{a21} and κ_{b12} . Therefore, in the experiments, we chose a microdisk with more surface roughness to induce larger backscattering and a microtoroid with a significant reflection signal. Second, the decay rate of level $\omega_{1,\mathrm{EP}+}$ should be much smaller than that of level $\omega_{2,\pm}$ in analogy to the longer lifetime of the metastable state in atomic EIT. This is satisfied by choosing highly dissimilar quality factors for the modes in the two resonators that allow $\gamma_{0,1} \ll \gamma_{0,2}$.

When μR_1 is strongly coupled to the taper (that is, $\gamma_{1,1} \gg \gamma_{0,1}$) and μR_2 is critically coupled to the fibre taper (that is, $\gamma_{1,2} \approx \gamma_{0,2}$), the transmission at the zero detuning point $\Delta = 0$ is given by (detailed calculation in Supplementary Section A2):

$$T(\Delta = 0) = \left| \frac{1}{1 + \frac{4\gamma_{1,2}\kappa_{2,1}e^{2i\theta}}{\gamma_{1,1}\kappa_{2,1}} + \frac{\gamma_{1,2}^2}{\kappa_{2,1}\kappa_{2,1}}} \right|^2 \tag{7}$$

Ideally, the transmission gets close to 1 when $|4\kappa_{a21}\kappa_{b12}/\gamma_{1,1}\gamma_{1,2}| \rightarrow 1$, which means that the last two terms in the denominator will cancel with a proper value of θ . Under our experimental condition, $|4\kappa_{a21}\kappa_{b12}/\gamma_{1,1}\gamma_{1,2}|$ is much smaller than 1 due to the limitation in the backscattering rates.

In the experiments, we study the transmission spectrum controlled by the two types of chiral eigenstate of μR_1 associated with EP_ and EP_. We first tune μR_1 to EP_, which is verified by checking that the reflection signal is zero as the light is injected from the

right port (Fig. 3a). The lack of necessary backscattering ($\kappa_{a21} = 0$) eliminates loop interference and gives rise to the exhibition of two overlapping dips with highly different linewidths in the transmission spectrum (Fig. 3b). The interpretation of this phenomenon is similar to the 'superscattering' phenomenon where the partial scattering cross-sections into uncoupled channels are added without interference⁴²⁻⁴⁴. The narrow absorption dip occurring at EP_ is also found to be invariant with the phase shift θ (Fig. 3c), consistent with our theoretical prediction (Fig. 3d). Moreover, the depth of the narrow dip varies with the change of coupling strength between μR_1 and the fibre taper (see Supplementary Section C3 for more details). In this phase-invariant opaqueness, the energy loss is mainly the absorption loss, together with a minor portion of scattering loss into free space and reflection into the backward channel of the fibre. Therefore, these results verify that the -1 chiral state at EP_ leads to a phaseinvariant type of absorption, which we name exceptional-pointassisted absorption (EPAA). It is noted that EPAA is fundamentally different from electromagnetically induced absorption^{4,45,46}, which relies on constructive interference. For EPAA, the absence of interference, which is critical for the superscattering type of absorption, is ensured by EP_ regardless of the backscattering ubiquitously existing in high-Q WGM resonators. This superscattering phenomenon achieves a large cross-section for light absorption and thus enhances light-matter interaction and energy harvest, which can further benefit applications such as antenna design and biomedical imaging^{43,44}.

At EP₊, with properly chosen θ controlled by the distance between resonators, we observe a single narrow peak out of a broad absorption

ARTICLES NATURE PHYSICS

in the transmission spectrum (Fig. 4a, upper panel). The pure transparency lineshape appears only when the coupling strength between $\mu R_{\scriptscriptstyle 1}$ and the taper is strong (see Supplementary Section C3 for simulation results). To demonstrate this, we increase $\gamma_{1,1}$ by reducing the gap between μR_1 and the taper in 50 nm steps, and the narrow dip in the transmission spectrum gradually evolves into a narrow peak (Fig. 4c). Furthermore, to verify that the transparency window is associated with the destructive interference in the optical loop, we control the phase θ by tuning the horizontal distance between μR_1 and μR_2 . The height of the peak in the transmission spectrum ($\Delta = 0$) is modified with the variation of the distance (Fig. 4a), a hallmark of an interference effect. In theory, when the phase shift is optimized $(\theta = \theta_{opt})$, the peak reaches its highest point, corresponding to destructive interference (Fig. 4b). When the phase shift deviates from the optimized value, the peak goes downward. The deepest absorption dip appears at an angle of $\theta_{opt} + \pi/2$, where the term $\gamma_{1,1}\gamma_{1,2}\kappa_{a21}\kappa_{b12}e^{2i\theta}$ is opposite to that under the optimized phase, corresponding to constructive interference in the optical loop. In addition, as two eigenstates of μR_1 coalesce at EP₊, the transparency window under destructive interference has a single peak, which we name as exceptional-point-assisted transparency. For a general non-EP case, the system-level structure (Fig. 2a) can support multiple EIT processes and is likely to induce splitting in the transparency window due to multiple resonances (Supplementary Section C1).

Our experiments demonstrate that the chiral state in μR_1 can be effectively coupled to the standing-wave modes in μR_2 only when the chirality is 1. In other words, the chiral mode has a preferred direction of coupling: it can be coupled to the mode only in its forward-propagation path. Moreover, we note that the backward transmission signal (with the probing laser injected into the right port) is exactly the same due to the reciprocity of the system, further verifying that the direction of coupling associated with chirality is invariant with probing directions.

As we have seen so far, the chirality of EPs could be utilized to tailor the light transport and interference in a waveguide-coupled resonator system, and thus has great potential in the generation and control of slow light. In integrated photonic structures, the EPs can be achieved by index modulation or geometry deformation (for example, EP modulation in an InGaAsP integrated ring resonator platform with periodically arranged Ge and Cr/Ge)²⁶. The recent development of LiNbO3 fabrication technology enables robust refractive index modulation in microdisks via digital electrical signals^{47,48} or complementary metal-oxide-semiconductor-compatible voltages⁴⁸. Those techniques compatible with integrated photonic platforms have the potential for robustly steering a microdisk to two types of EPs with chirality -1 and 1, and overcoming the thermal noise and non-equilibrium problems in conventional methods. Hence, the chirality of EPs could help realize state-controlled EIT with a high operation rate and fidelity.

Online content

Any methods, additional references, Nature Research reporting summaries, source data, extended data, supplementary information, acknowledgements, peer review information; details of author contributions and competing interests; and statements of data and code availability are available at https://doi.org/10.1038/s41567-019-0746-7.

Received: 24 May 2019; Accepted: 11 November 2019; Published online: 13 January 2020

References

- Fleischhauer, M., Imamoglu, A. & Marangos, J. P. Electromagnetically induced transparency: optics in coherent media. *Rev. Mod. Phys.* 77, 633–673 (2005).
- Project, P. et al. Nonlinear optical processes using electromagnetically induced transparency. *Phys. Rev. Lett.* 64, 1107–1110 (1990).

- Boller, K. J., Imamoğlu, A. & Harris, S. E. Observation of electromagnetically induced transparency. *Phys. Rev. Lett.* 66, 2593–2596 (1991).
- Akulshin, A. M., Barreiro, S. & Lezama, A. Electromagnetically induced absorption and transparency due to resonant two-field excitation of quasidegenerate levels in Rb vapor. *Phys. Rev. A* 57, 2996–3002 (1998).
- Röhlsberger, R., Wille, H.-C., Schlage, K. & Sahoo, B. Electromagnetically induced transparency with resonant nuclei in a cavity. *Nature* 482, 199–203 (2012).
- Mücke, M. et al. Electromagnetically induced transparency with single atoms in a cavity. Nature 465, 755–758 (2010).
- Papasimakis, N., Fedotov, V. A., Prosvirnin, S. L. & Zheludev, N. I. A metamaterial analog of electromagnetically induced transparency. *Phys. Rev. Lett.* 101, 253903 (2008).
- Jain, A. et al. Electromagnetically induced transparency and absorption in metamaterials: the radiating two-oscillator model and its experimental confirmation. *Phys. Rev. Lett.* 109, 187401 (2012).
- Liu, N. et al. Plasmonic analogue of electromagnetically induced transparency at the Drude damping limit. Nat. Mater. 8, 758–762 (2009).
- Taubert, R., Hentschel, M., Kästel, J. & Giessen, H. Classical analog of electromagnetically induced absorption in plasmonics. *Nano Lett.* 12, 1367–1371 (2012).
- Dyer, G. C. et al. Induced transparency by coupling of Tamm and defect states in tunable terahertz plasmonic crystals. Nat. Photon. 7, 925–930 (2013).
- Hsu, C. W., DeLacy, B. G., Johnson, S. G., Joannopoulos, J. D. & Soljacic, M. Theoretical criteria for scattering dark states in nanostructured particles. *Nano Lett.* 14, 2783–2788 (2014).
- 13. Xu, Q. et al. Experimental realization of an on-chip all-optical analogue to electromagnetically induced transparency. *Phys. Rev. Lett.* **96**, 123901 (2006).
- Xu, Q., Dong, P. & Lipson, M. Breaking the delay-bandwidth limit in a photonic structure. Nat. Phys. 3, 406–410 (2007).
- Limonov, M. F., Rybin, M. V., Poddubny, A. N. & Kivshar, Y. S. Fano resonances in photonics. *Nat. Photon.* 11, 543–554 (2017).
- Weis, S. et al. Optomechanically induced transparency. Science 330, 1515–1520 (2010).
- Safavi-Naeini, A. H. et al. Electromagnetically induced transparency and slow light with optomechanics. *Nature* 472, 69–73 (2011).
- Lü, H., Wang, C., Yang, L. & Jing, H. Optomechanically induced transparency at exceptional points. Phys. Rev. Appl. 10, 14006 (2018).
- Anisimov, P. M., Dowling, J. P. & Sanders, B. C. Objectively discerning Autler-Townes splitting from electromagnetically induced transparency. *Phys. Rev. Lett.* 107, 163604 (2011).
- Abdumalikov, A. A. et al. Electromagnetically induced transparency on a single artificial atom. *Phys. Rev. Lett.* 104, 193601 (2010).
- 21. Veldhorst, M. et al. A two-qubit logic gate in silicon. *Nature* **526**, 410–414 (2015).
- Li, X. et al. An all-optical quantum gate in a semiconductor quantum dot. Science 301, 809–811 (2003).
- Pang, M., He, W., Jiang, X. & Russell, P. S. J. All-optical bit storage in a fibre laser by optomechanically bound states of solitons. *Nat. Photon.* 10, 454–458 (2016).
- Wu, B. et al. Slow light on a chip via atomic quantum state control. Nat. Photon. 4, 776–779 (2010).
- Peng, B. et al. Chiral modes and directional lasing at exceptional points. Proc. Natl Acad. Sci. USA 113, 6845–6850 (2016).
- Miao, P. et al. Orbital angular momentum microlaser. Science 353, 464–467 (2016).
- Cao, H. & Wiersig, J. Dielectric microcavities: model systems for wave chaos and non-Hermitian physics. Rev. Mod. Phys. 87, 61–111 (2015).
- El-Ganainy, R. et al. Non-Hermitian physics and PT symmetry. Nat. Phys. 14, 11–19 (2018).
- Feng, L., El-Ganainy, R. & Ge, L. Non-Hermitian photonics based on parity-time symmetry. *Nat. Photon.* 11, 752–762 (2017).
- Miri, M.-A. & Alù, A. Exceptional points in optics and photonics. Science 363, eaar7709 (2019).
- Feng, L. et al. Experimental demonstration of a unidirectional reflectionless parity-time metamaterial at optical frequencies. Nat. Mater. 12, 108–113 (2013).
- Chen, W., Kaya Özdemir, Ş., Zhao, G., Wiersig, J. & Yang, L. Exceptional points enhance sensing in an optical microcavity. *Nature* 548, 192–196 (2017).
- 33. Hodaei, H. et al. Enhanced sensitivity at higher-order exceptional points. *Nature* **548**, 187–191 (2017).
- Xu, H., Mason, D., Jiang, L. & Harris, J. G. E. Topological energy transfer in an optomechanical system with exceptional points. *Nature* 537, 80–83 (2016).
- 35. Hahn, C. et al. Time-asymmetric loop around an exceptional point over the full optical communications band. *Nature* **562**, 86–90 (2018).
- Zhang, J. et al. A phonon laser operating at an exceptional point. *Nat. Photon.* 12, 479–484 (2018).
- 37. Wong, Z. J. et al. Lasing and anti-lasing in a single cavity. Nat. Photon. 10, 796-801 (2016).

NATURE PHYSICS ARTICLES

- Zhao, H. et al. Metawaveguide for asymmetric interferometric light-light switching. Phys. Rev. Lett. 117, 193901 (2016).
- Peng, B. et al. Parity-time-symmetric whispering-gallery microcavities. Nat. Phys. 10, 394–398 (2014).
- 40. Peng, B. et al. Loss-induced suppression and revival of lasing. *Science* **346**, 328–332 (2014).
- 41. Liu, Y.-C., Li, B.-B. & Xiao, Y.-F. Electromagnetically induced transparency in optical microcavities. *Nanophotonics* **6**, 789–811 (2017).
- 42. Ruan, Z. & Fan, S. Superscattering of light from subwavelength nanostructures. *Phys. Rev. Lett.* **105**, 013901 (2010).
- 43. Verslegers, L., Yu, Z., Ruan, Z., Catrysse, P. B. & Fan, S. From electromagnetically induced transparency to superscattering with a single structure: a coupled-mode theory for doubly resonant structures. *Phys. Rev. Lett.* **108**, 083902 (2012).
- 44. Qian, C. et al. Experimental observation of superscattering. *Phys. Rev. Lett.* 122, 063901 (2019).
- 45. Lezama, A., Barreiro, S. & Akulshin, A. M. Electromagnetically induced absorption. *Phys. Rev. A* **59**, 4732–4735 (1999).
- Taichenachev, A. V., Tumaikin, A. M. & Yudin, V. I. Electromagnetically induced absorption in a four-state system. *Phys. Rev. A* 61, 011802 (1999).
- 47. Zhang, M. et al. Broadband electro-optic frequency comb generation in an integrated microring resonator. *Nature* **568**, 373–377 (2018).
- Wang, C. et al. Integrated lithium niobate electro-optic modulators operating at CMOS-compatible voltages. *Nature* 562, 101–104 (2018).

Acknowledgements

This work was supported by NSF grant no. EFMA1641109, ARO grant no. W911NF1710189 and DARPA under grant HR00111820042. A.D.S. acknowledges the support of NSF grant no. DMR-1743235. L.J. acknowledges the support of the Packard Foundation (2013-39273).

Author contributions

X.J., C.W. and L.Y. conceived the idea and designed the experiments. C.W. and X.J. performed the experiments with help from G.Z. and B.P. C.W. analysed experimental data with help from X.J. and M.Z. Theoretical background and simulations were provided by C.W. with help from M.Z., C.W.H., L.J. and A.D.S. All authors discussed the results and wrote the manuscript. L.Y. supervised the project.

Competing interests

The authors declare no competing interests.

Additional information

Supplementary information is available for this paper at https://doi.org/10.1038/s41567-019-0746-7.

Correspondence and requests for materials should be addressed to L.Y.

Reprints and permissions information is available at www.nature.com/reprints.

Publisher's note Springer Nature remains neutral with regard to jurisdictional claims in published maps and institutional affiliations.

© The Author(s), under exclusive licence to Springer Nature Limited 2020

ARTICLES NATURE PHYSICS

(8)

Methods

Theoretical framework under the experimental condition. We consider the specific situation where the intrinsic perturbations are induced by nanoparticles and the external perturbation is induced by a nanotip 15,32,49,30 . Besides the intermodal coupling within a resonator, the perturbations induce mode shift and linewidth broadening that were not explicitly specified in the ideal model equations (1)-(4). With these factors taken into consideration, the coupled mode equations are given by:

$$\frac{\mathrm{d}}{\mathrm{d}t} \begin{pmatrix} a_1 \\ a_2 \end{pmatrix} = \begin{pmatrix} -i\omega_1 - \frac{\gamma_{0,1} + \gamma_{1,1}}{2} - i\varepsilon_{a1} - i\varepsilon_{a2} & -i(\varepsilon_{a1} \mathrm{e}^{-i2m_a\beta_{a1}} + \varepsilon_{a2}\mathrm{e}^{-i2m_a\beta_{a2}}) \\ -i(\varepsilon_{a1}\mathrm{e}^{i2m_a\beta_{a1}} + \varepsilon_{a2}\mathrm{e}^{i2m_a\beta_{a2}}) & -i\omega_1 - \frac{\gamma_{0,1} + \gamma_{1,1}}{2} - i\varepsilon_{a1} - i\varepsilon_{a2} \end{pmatrix} \begin{pmatrix} a_1 \\ a_2 \end{pmatrix} \\ -\sqrt{\gamma_{1,1}} \begin{pmatrix} a_{\mathrm{in}} \\ \mathrm{e}^{i\theta} \sqrt{\gamma_{1,2}} b_2 \end{pmatrix}$$

$$\frac{\mathrm{d}}{\mathrm{d}i} \begin{pmatrix} b_1 \\ b_2 \end{pmatrix} = \begin{pmatrix} -i\omega_2 - \frac{\gamma_{0,2} + \gamma_{1,2}}{2} - i\varepsilon_b & -i\varepsilon_b e^{-i2m_b\beta_b} \\ -i\varepsilon_b e^{i2m_b\beta_b} & -i\omega_2 - \frac{\gamma_{0,2} + \gamma_{1,2}}{2} - i\varepsilon_b \end{pmatrix} \begin{pmatrix} b_1 \\ b_2 \end{pmatrix} - \sqrt{\gamma_{1,2}} e^{i\theta} \begin{pmatrix} a_{\mathrm{in}} + \sqrt{\gamma_{1,1}} a_1 \\ 0 \end{pmatrix}$$
(9)

We define the effective resonant frequencies as $\omega_1' = \omega_1 - \text{Re}(\epsilon_{a1}) - \text{Re}(\epsilon_{a2})$ and $\omega_2' = \omega_2 - \text{Re}(\epsilon_b)$, and redefine the frequency detuning as

 $\Delta_1 = \omega - \omega_1 - \text{Re}(\epsilon_{a1}) - \text{Re}(\epsilon_{a2})$ and $\Delta_2 = \omega - \omega_2 - \text{Re}(\epsilon_b)$. Taking $\Delta_1 = \Delta_2 = \Delta$, the result of transmission is given by:

$$T = \frac{\left[\left[-(\gamma_{0,1}^{\prime} - 2i\Delta)^{2} + \gamma_{1,1}^{2} - 4\kappa_{a21}\kappa_{a12} \right] \left[-(\gamma_{0,2}^{\prime} - 2i\Delta)^{2} + \gamma_{1,2}^{2} - 4\kappa_{b21}\kappa_{b12} \right] \right]^{2}}{P + \left[(\gamma_{0,1}^{\prime} + \gamma_{1,1} - 2i\Delta)^{2} + 4\kappa_{a21}\kappa_{a12} \right] \left[(\gamma_{0,2}^{\prime} + \gamma_{1,2} - 2i\Delta)^{2} + 4\kappa_{b21}\kappa_{b12} \right]}$$
(10)

where $P=16\gamma_{1,1}\gamma_{1,2}\kappa_{a21}\kappa_{b12}{\bf e}^{2i\theta}$, and effective loss rates $\gamma'_{0,1}=\gamma_{0,1}-2{\rm Im}(\epsilon_{a1}+\epsilon_{a2})$ and $\gamma'_{0,2}=\gamma_{0,2}-2{\rm Im}(\epsilon_b)$. This result is exactly the same as equation (6) except that we have explicitly included the mode-broadening effect induced by perturbations. The frequency shifts can be cancelled by adjusting the detuning frequency between the two resonators, and thus have no effect on the experimental results.

Data availability

The data represented in Figs. 1–4 are available in Supplementary Data 1–4. All other data that support the plots within this paper and other findings of this study are available from the corresponding author upon reasonable request.

References

- Zhu, J., Özdemir, Ş. K., He, L. & Yang, L. Controlled manipulation of mode splitting in an optical microcavity by two Rayleigh scatterers. *Opt. Express* 18, 23535–23543 (2010).
- Zhu, J. et al. On-chip single nanoparticle detection and sizing by mode splitting in an ultrahigh-Q microresonator. Nat. Photon. 4, 46–49 (2010).



SUPPLEMENTARY INFORMATION

https://doi.org/10.1038/s41567-019-0746-7

In the format provided by the authors and unedited.

Electromagnetically induced transparency at a chiral exceptional point

Changqing Wang^{1,7}, Xuefeng Jiang^{1,7}, Guangming Zhao¹, Mengzhen Zhang^{2,3}, Chia Wei Hsu^{0,2,3,4}, Bo Peng^{1,6}, A. Douglas Stone^{2,3}, Liang Jiang^{0,2,3,5} and Lan Yang^{0,1*}

¹Department of Electrical and Systems Engineering, Washington University, St Louis, MO, USA. ²Departments of Applied Physics and Physics, Yale University, New Haven, CT, USA. ³Yale Quantum Institute, Yale University, New Haven, CT, USA. ⁴Ming Hsieh Department of Electrical and Computer Engineering, University of Southern California, Los Angeles, CA, USA. ⁵Pritzker School of Molecular Engineering, University of Chicago, Chicago, IL, USA. ⁶Present address: Globalfoundries, East Fishkill, NY, USA. ⁷These authors contributed equally: Changqing Wang, Xuefeng Jiang. *e-mail: yang@seas.wustl.edu

Supplementary Information – Electromagnetically induced transparency at a chiral exceptional point

Changqing Wang^{1,7}, Xuefeng Jiang^{1,7}, Guangming Zhao¹, Mengzhen Zhang^{2,3}, Chia Wei Hsu^{2,3,4}, Bo Peng^{1,6}, A. Douglas Stone^{2,3}, Liang Jiang^{2,3,5} and Lan Yang^{1*}

¹Department of Electrical and Systems Engineering, Washington University, St Louis, MO, USA.

²Departments of Applied Physics and Physics, Yale University, New Haven, CT, USA.

³Yale Quantum Institute, Yale University, New Haven, CT, USA.

⁴Ming Hsieh Department of Electrical and Computer Engineering, University of Southern California, Los Angeles, CA, USA.

⁵Pritzker School of Molecular Engineering, University of Chicago, Chicago, IL, USA.

⁶Present address: Globalfoundries, East Fishkill, NY, USA.

⁷These authors contributed equally: Changqing Wang and Xuefeng Jiang.

*e-mail: yang@seas.wustl.edu

A. Theoretical model of EPAT & EPAA

A1. General model

We provide a theoretical model describing the system of indirectly coupled microresonators based on the coupled mode theory¹. The configuration describing the system is shown in the diagram in Fig. S1. We consider both clockwise and counterclockwise modes for the left microresonator μR_1 and the right resonator μR_2 , respectively, with the intracavity mode fields $a_{1,2}$ and $b_{1,2}$. The two resonators have resonant frequencies marked by $\omega_{1,2}$ and intrinsic loss rates $\gamma_{0,1}$ and $\gamma_{0,2}$, respectively. Due to the existence of intrinsic or external perturbations, a_1 and a_2 are coupled by coupling strengths κ_{a12} and κ_{a21} , and b_1 and b_2 are coupled by coupling strengths κ_{b12} and κ_{b21} . The field amplitudes in each port are given by a_{in} , a'_{out} , $e^{i\theta}a'_{out}$, a_{out} , b_{in} , b'_{out} , $e^{i\theta}b'_{out}$ and b_{out} , as shown in the diagram. The resonators are coupled to the same fibre taper by the coupling strengths $\gamma_{1,1}$ and $\gamma_{1,2}$, respectively. The dynamics of the field amplitudes are described by the coupled mode theory²⁻⁴.

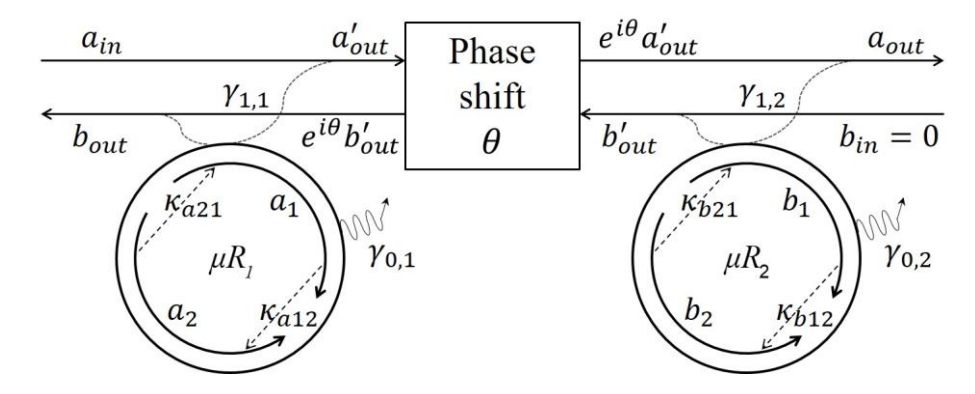


Fig. S1 | Schematic diagram of the indirectly coupled resonators. The resonators support clockwise and counterclockwise modes, respectively, and are coupled to the same fibre taper. There are forward and backward channels of light flow in the taper which are plotted separately by the forward and backward arrow lines. Light travelling in the taper by the distance between the resonators will have a phase shift θ .

$$\frac{d}{dt} \binom{a_1}{a_2} = \begin{pmatrix} -i\omega_1 - \frac{\gamma_{0,1} + \gamma_{1,1}}{2} & -i\kappa_{a21} \\ -i\kappa_{a12} & -i\omega_1 - \frac{\gamma_{0,1} + \gamma_{1,1}}{2} \end{pmatrix} \binom{a_1}{a_2} - \sqrt{\gamma_{1,1}} \binom{a_{in}}{e^{i\theta}b'_{out}}, \tag{S1}$$

$$\begin{pmatrix} a'_{out} \\ b_{out} \end{pmatrix} - \begin{pmatrix} a_{in} \\ e^{i\theta} b'_{out} \end{pmatrix} = \sqrt{\gamma_{1,1}} \begin{pmatrix} a_1 \\ a_2 \end{pmatrix}$$
 (S2)

$$\frac{d}{dt} \binom{b_1}{b_2} = \begin{pmatrix} -i\omega_2 - \frac{\gamma_{0,2} + \gamma_{1,2}}{2} & -i\kappa_{b21} \\ -i\kappa_{b12} & -i\omega_2 - \frac{\gamma_{0,2} + \gamma_{1,2}}{2} \end{pmatrix} \binom{b_1}{b_2} - \sqrt{\gamma_{1,2}} \binom{e^{i\theta}a'_{out}}{0}, \tag{S3}$$

$$\binom{a_{out}}{b'_{out}} - \binom{e^{i\theta}a'_{out}}{0} = \sqrt{\gamma_{1,2}} \binom{b_1}{b_2}.$$
 (S4)

By converting Eqs. (S1)-(S4) into the frequency domain, we obtain

$$0 = \begin{pmatrix} i\Delta_{1} - \frac{\gamma_{0,1} + \gamma_{1,1}}{2} & -i\kappa_{a21} \\ -i\kappa_{a12} & i\Delta_{1} - \frac{\gamma_{0,1} + \gamma_{1,1}}{2} \end{pmatrix} \begin{pmatrix} a_{1}[\omega] \\ a_{2}[\omega] \end{pmatrix} - \sqrt{\gamma_{1,1}} \begin{pmatrix} a_{in}[\omega] \\ e^{i\theta} b'_{out}[\omega] \end{pmatrix}, \tag{S5}$$

$$\begin{pmatrix} a'_{out}[\omega] \\ b_{out}[\omega] \end{pmatrix} - \begin{pmatrix} a_{in}[\omega] \\ e^{i\theta} b'_{out}[\omega] \end{pmatrix} = \sqrt{\gamma_{1,1}} \begin{pmatrix} a_1[\omega] \\ a_2[\omega] \end{pmatrix},$$
 (S6)

$$0 = \begin{pmatrix} i\Delta_{2} - \frac{\gamma_{0,2} + \gamma_{1,2}}{2} & -i\kappa_{b21} \\ -i\kappa_{b12} & i\Delta_{2} - \frac{\gamma_{0,2} + \gamma_{1,2}}{2} \end{pmatrix} \begin{pmatrix} b_{1}[\omega] \\ b_{2}[\omega] \end{pmatrix} - \sqrt{\gamma_{1,2}} \begin{pmatrix} e^{i\theta} \alpha'_{out}[\omega] \\ 0 \end{pmatrix}, \tag{S7}$$

$$\begin{pmatrix} a_{out}[\omega] \\ b'_{out}[\omega] \end{pmatrix} - \begin{pmatrix} e^{i\theta} a'_{out}[\omega] \\ 0 \end{pmatrix} = \sqrt{\gamma_{1,2}} \begin{pmatrix} b_1[\omega] \\ b_2[\omega] \end{pmatrix},$$
 (S8)

where $\Delta_1 = \omega - \omega_1$, $\Delta_2 = \omega - \omega_2$, and $x[\omega]$ represents the Fourier transform of x (x can be a_{in} , a'_{out} , a_{out} , b_{in} , b'_{out} , b_{out} , a_1 , a_2 , b_1 or b_2). By solving Eqs. (S5)-(S8), we obtain the transmission spectrum as

$$T = |t|^2 = \left| \frac{a_{out}[\omega]}{a_{in}[\omega]} \right|^2 = \left| (S_1)_{1,1} (S_2)_{1,1} \left\{ 1 + (S_1)_{1,2} (S_2)_{2,1} \left[1 - (S_2)_{2,1} (S_1)_{1,2} \right]^{-1} \right\} \right|^2, \tag{S9}$$

where

$$S_{1} = \begin{pmatrix} 1 - \frac{2i\gamma_{1,1}\left(\gamma_{0,1} + \gamma_{1,1} - 2i\Delta_{1}\right)}{i\left(\gamma_{0,1} + \gamma_{1,1} - 2i\Delta_{1}\right)^{2} + 4i\kappa_{a21}\kappa_{a12}} & -\frac{4\gamma_{1,1}\kappa_{a21}e^{i\theta}}{i\left(\gamma_{0,1} + \gamma_{1,1} - 2i\Delta_{1}\right)^{2} + 4i\kappa_{a21}\kappa_{a12}} \\ -\frac{4\gamma_{1,1}\kappa_{a12}}{i\left(\gamma_{0,1} + \gamma_{1,1} - 2i\Delta_{1}\right)^{2} + 4i\kappa_{a21}\kappa_{a12}} & e^{i\theta} - \frac{2i\gamma_{1,1}\left(\gamma_{0,1} + \gamma_{1,1} - 2i\Delta_{1}\right)e^{i\theta}}{i\left(\gamma_{0,1} + \gamma_{1,1} - 2i\Delta_{1}\right)^{2} + 4i\kappa_{a21}\kappa_{a12}} \end{pmatrix}, (S10)$$

$$S_{2} = \begin{pmatrix} e^{i\theta} - \frac{2i\gamma_{1,2}(\gamma_{0,2} + \gamma_{1,2} - 2i\Delta_{2})e^{i\theta}}{i(\gamma_{0,2} + \gamma_{1,2} - 2i\Delta_{2})^{2} + 4i\kappa_{b21}\kappa_{b12}} & -\frac{4\gamma_{1,2}\kappa_{b21}}{i(\gamma_{0,2} + \gamma_{1,2} - 2i\Delta_{2})^{2} + 4i\kappa_{b21}\kappa_{b12}} \\ -\frac{4\gamma_{1,2}\kappa_{b12}e^{i\theta}}{i(\gamma_{0,2} + \gamma_{1,2} - 2i\Delta_{2})^{2} + 4i\kappa_{b21}\kappa_{b12}} & 1 - \frac{2i\gamma_{1,2}(\gamma_{0,2} + \gamma_{1,2} - 2i\Delta_{2})}{i(\gamma_{0,2} + \gamma_{1,2} - 2i\Delta_{2})^{2} + 4i\kappa_{b21}\kappa_{b12}} \end{pmatrix}. (S11)$$

We assume the resonant frequency detuning between two resonators is zero, i.e., $\Delta_1 = \Delta_2 = \Delta$. Then we obtain the transmission spectrum as

$$T = \left| \frac{\left(-\left(\gamma_{0,1} - 2i\Delta \right)^2 + \gamma_{1,1}^2 - 4\kappa_{a21}\kappa_{a12} \right) \left(-\left(\gamma_{0,2} - 2i\Delta \right)^2 + \gamma_{1,2}^2 - 4\kappa_{b21}\kappa_{b12} \right)}{16\gamma_{1,1}\gamma_{1,2}\kappa_{a21}\kappa_{b12}e^{2i\theta} + \left(\left(\gamma_{0,1} + \gamma_{1,1} - 2i\Delta \right)^2 + 4\kappa_{a21}\kappa_{a12} \right) \left(\left(\gamma_{0,2} + \gamma_{1,2} - 2i\Delta \right)^2 + 4\kappa_{b21}\kappa_{b12} \right)} \right|^2.$$
(S12)

From here, it is obvious that the term $16\gamma_{1,1}\gamma_{1,2}\kappa_{a21}\kappa_{b12}e^{2i\theta}$ plays the critical role of inducing interference effect which could lead to a transparency window out of a wide dip in either EIT or EPAT case. Without this term, the transmission will be decoupled to cascaded coupling between a taper and two resonators, given by

$$T = \left| \frac{\left(-\left(\gamma_{0,1} - 2i\Delta \right)^2 + \gamma_{1,1}^2 - 4\kappa_{a21}\kappa_{a12} \right) \left(-\left(\gamma_{0,2} - 2i\Delta \right)^2 + \gamma_{1,2}^2 - 4\kappa_{b21}\kappa_{b12} \right)}{\left(\left(\gamma_{0,1} + \gamma_{1,1} - 2i\Delta \right)^2 + 4\kappa_{a21}\kappa_{a12} \right) \left(\left(\gamma_{0,2} + \gamma_{1,2} - 2i\Delta \right)^2 + 4\kappa_{b21}\kappa_{b12} \right)} \right|^2.$$
 (S13)

And thus no interference effect will happen.

We discuss different cases when the chirality of μR_1 is tuned, from which we can see the effect of the loop coupling coefficient $16\gamma_{1.1}\gamma_{1.2}\kappa_{a21}\kappa_{b12}e^{2i\theta}$.

- 1) μR_1 is only subject to intrinsic perturbations and the chirality is not broken. Therefore κ_{a21} , κ_{a12} , κ_{b21} and κ_{b12} are all nonzero. Under the condition $\gamma_{1,2} \sim \gamma_{0,2}$ and $\gamma_{1,1} \leq \gamma_{0,1}$, we observe EIA with splitting (results shown in Section C1 in Supplementary Information). Under the condition $\gamma_{1,2} \sim \gamma_{0,2}$ and $\gamma_{1,1} \gg \gamma_{0,1}$, we are able to observe EIT with splitting.
- 2) μR_1 is tuned to the exceptional point with chirality -1 (EP₋), *i.e.*, $\kappa_{a21} = 0$. The term $16\gamma_{1,1}\gamma_{1,2}\kappa_{a21}\kappa_{b12}e^{2i\theta}$ vanishes. The two resonators are decoupled and the transmission will give rise to EPAA, a narrow dip out of a broad dip, in all coupling regimes.
- 3) μR_1 is tuned to the exceptional point with chirality 1 (EP₊), *i.e.*, $\kappa_{a12} = 0$. The term $16\gamma_{1,1}\gamma_{1,2}\kappa_{a21}\kappa_{b12}e^{2i\theta}$ is nonzero. The interference effect could lead to EPAT under certain coupling conditions described in the main text.

A2. Theoretical limit of the peak in EPAT

We study the zero detuning point $\Delta = 0$, at which the transmission becomes

$$T = \left| \frac{\left(-\gamma_{0,1}^2 + \gamma_{1,1}^2 - 4\kappa_{a21}\kappa_{a12} \right) \left(-\gamma_{0,2}^2 + \gamma_{1,2}^2 - 4\kappa_{b21}\kappa_{b12} \right)}{16\gamma_{1,1}\gamma_{1,2}\kappa_{a21}\kappa_{b12}e^{2i\theta} + \left(\left(\gamma_{0,1} + \gamma_{1,1} \right)^2 + 4\kappa_{a21}\kappa_{a12} \right) \left(\left(\gamma_{0,2} + \gamma_{1,2} \right)^2 + 4\kappa_{b21}\kappa_{b12} \right)} \right|^2.$$
 (S14)

We first set the low-Q resonator to be critically coupled to the fibre taper, i.e., $\gamma_{1,2} \approx \gamma_{0,2}$, which yields

$$T = \left| \frac{\left(-\gamma_{0,1}^2 + \gamma_{1,1}^2 - 4\kappa_{a21}\kappa_{a12} \right) \kappa_{b21}\kappa_{b12}}{4\gamma_{1,1}\gamma_{1,2}\kappa_{a21}\kappa_{b12} e^{2i\theta} + \left(\left(\gamma_{0,1} + \gamma_{1,1} \right)^2 + 4\kappa_{a21}\kappa_{a12} \right) \left(\gamma_{1,2}^2 + \kappa_{b21}\kappa_{b12} \right)} \right|^2.$$
 (S15)

At EP₊, $\kappa_{a12} = 0$. Furthermore, if the coupling strength between the high-Q resonator and the taper is strong, i.e., $\gamma_{1,1} \gg \gamma_{0,1}$, $\sqrt{4\kappa_{a21}\kappa_{a12}}$, then

$$T = \left| \frac{\gamma_{1,1} \kappa_{b21} \kappa_{b12}}{4 \gamma_{1,2} \kappa_{a21} \kappa_{b12} e^{2i\theta} + \gamma_{1,1} \gamma_{1,2}^2 + \gamma_{1,1} \kappa_{b21} \kappa_{b12}} \right|^2.$$
 (S16)

The transmission gets close to 1 when the following condition is satisfied

$$\kappa_{a21}\kappa_{b12}e^{2i\theta} = -\gamma_{1,1}\gamma_{1,2}/4.$$
(S17)

Thus with properly chosen parameters, it is theoretically possible to see a high narrow peak with $T \to 1$ emerging out of a broad dip. We thus summarize the condition to have a higher peak of transparency at $\Delta = 0$ when the low-Q resonator is nearly critically coupled to the taper:

1) The high-Q resonator has a quality factor significantly larger than the low-Q resonator.

- 2) The high-Q resonator is overcoupled to the taper, i.e., $\gamma_{1,1} \gg \gamma_{0,1}$.
- 3) The coupling strength between μR_1 and the taper is much larger than the average coupling rate between CW and CCW in μR_1 , i.e., $\gamma_{1,1} \gg \sqrt{4\kappa_{a21}\kappa_{a12}}$. This condition is naturally satisfied at EP₊ because $\kappa_{a12} = 0$.
- 4) The coupling term $\kappa_{a21}\kappa_{b12}$ has the amplitude close to $\gamma_{1,1}\gamma_{1,2}/4$, and the phase $\theta = \frac{1}{2}\arg(-\gamma_{1,1}\gamma_{1,2}/4\kappa_{a21}\kappa_{b12}) = \frac{1}{2}\arg(-1/\kappa_{a21}\kappa_{b12})$.

By numerically solving the equations under parameters satisfying the conditions above, we obtain the estimated EPAT spectrum where the transmission at zero detuning approaches 1 (Fig. S2a). Also, as expected, the EPAT periodically changes with the phase θ , and only reaches the maximum when θ is properly chosen to match the phases of the terms $\kappa_{a21}\kappa_{b12}e^{2i\theta}$ and $-\gamma_{1,1}\gamma_{1,2}/4$ (Fig. S2b).

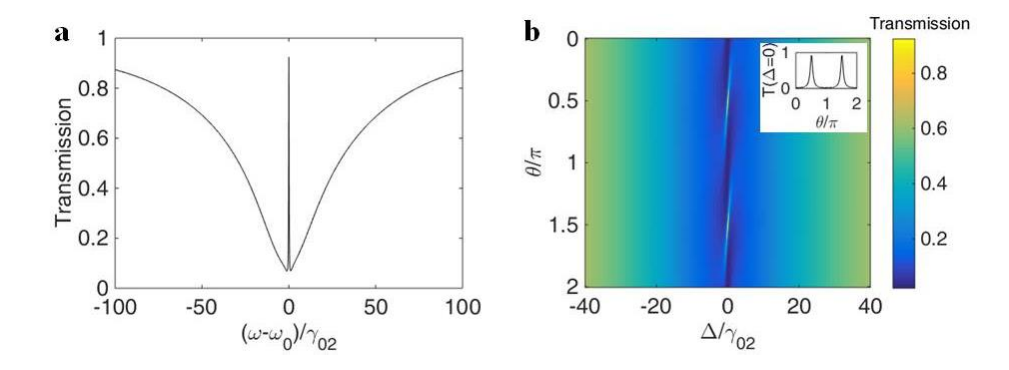


Fig. S2 | EPAT under the ideal conditions. a, Transmission spectrum at EP₊. Parameters: $\gamma_{0,1} = 21.69$, $\gamma_{0,2} = 5.33 \times 10^3$, $\kappa_{a21} = 11.79 + 74.31$ i, $\kappa_{a12} = 0$, $\kappa_{b21} = \kappa_{a12} = 1.30 \times 10^2 - 2.60 \times 10^3$ i, $\theta = 0.5171\pi$. b, Transmission spectrum at EP₊ with the variation of θ under the ideal conditions. Inset: transmission at $\Delta = 0$ vs. θ . Parameters are the same as in a except that θ is a variable.

A3. Model of the system under the experimental condition

The above analysis provides a general framework for transparency and absorption, but does not specify how the parameters κ_{a21} and κ_{a12} are determined in realistic systems. Under our experimental conditions, the intrinsic perturbations are induced by nanoparticles and the external perturbation is induced by a nanotip⁵. We use ϵ_{a1} and ϵ_{b} to denote the intrinsic perturbations on μR_1 and μR_2 respectively, and ϵ_{a2} to denote the external perturbation on μR_1 induced by the nanotip. The coupled mode equations are given by

$$\frac{d}{dt} \binom{a_1}{a_2} = \begin{pmatrix}
-i\omega_1 - \frac{\gamma_{0,1} + \gamma_{1,1}}{2} - i\epsilon_{a1} - i\epsilon_{a2} & -i(\epsilon_{a1}e^{-i2m_a\beta_{a1}} + \epsilon_{a2}e^{-i2m_a\beta_{a2}}) \\
-i(\epsilon_{a1}e^{i2m_a\beta_{a1}} + \epsilon_{a2}e^{i2m_a\beta_{a2}}) & -i\omega_1 - \frac{\gamma_{0,1} + \gamma_{1,1}}{2} - i\epsilon_{a1} - i\epsilon_{a2}
\end{pmatrix} \binom{a_1}{a_2} \\
-\sqrt{\gamma_{1,1}} \binom{a_{in}}{e^{i\theta}b'_{out}}, \tag{S18}$$

$$\frac{d}{dt} {b_1 \choose b_2} = \begin{pmatrix}
-i\omega_2 - \frac{\gamma_{0,2} + \gamma_{1,2}}{2} - i\varepsilon_b & -i\varepsilon_b e^{-i2m_b\beta_b} \\
-i\varepsilon_b e^{i2m_b\beta_b} & -i\omega_2 - \frac{\gamma_{0,2} + \gamma_{1,2}}{2} - i\varepsilon_b
\end{pmatrix} {b_1 \choose b_2} - \sqrt{\gamma_{1,2}} {e^{i\theta}\alpha'_{out} \choose 0}, \quad (S19)$$

where β_{a1} and β_{a2} are the azimuthal positions of the nanoscatters on μR_1 and β_b is the azimuthal position of the nanoscatter on μR_2 , with m_a and m_b being the azimuthal mode numbers of μR_1 and μR_2 , respectively. Incorporating Eqs. (S18)-(S19) with Eqs. (S2) and (S4), we can arrive at Eqs. (8)-(9) in the Methods. By defining $\omega_1' = \omega_1 - Re(\epsilon_{a1}) - Re(\epsilon_{a2})$, $\omega_2' = \omega_2 - Re(\epsilon_b)$, $\Delta_1 = \omega - \omega_1 - Re(\epsilon_{a1}) - Re(\epsilon_{a2})$, $\Delta_2 = \omega - \omega_2 - Re(\epsilon_b)$ and taking $\Delta_1 = \Delta_2 = \Delta$, we get

$$T = \left| \frac{\left(-\left(\gamma_{0,1}' - 2i\Delta \right)^2 + \gamma_{1,1}^2 - 4\kappa_{a21}\kappa_{a12} \right) \left(-\left(\gamma_{0,2}' - 2i\Delta \right)^2 + \gamma_{1,2}^2 - 4\kappa_{b21}\kappa_{b12} \right)}{P + \left(\left(\gamma_{0,1}' + \gamma_{1,1} - 2i\Delta \right)^2 + 4\kappa_{a21}\kappa_{a12} \right) \left(\left(\gamma_{0,2}' + \gamma_{1,2} - 2i\Delta \right)^2 + 4\kappa_{b21}\kappa_{b12} \right)} \right|^2, \tag{S20}$$

which is shown by Eq. (10) in the Methods, where $P = 16\gamma_{1,1}\gamma_{1,2}\kappa_{a21}\kappa_{b12}e^{2i\theta}$, $\gamma'_{0,1} = \gamma_{0,1} - 2Im(\epsilon_{a1} + \epsilon_{a2})$, $\gamma'_{0,2} = \gamma_{0,2} - 2Im(\epsilon_b)$.

Now the question is whether the peak of EPAT can get close to 1 under the real experimental conditions. To achieve this, perturbation for the high-Q resonator needs to have a large real part comparable to $\gamma_{1,1}$ and a small imaginary part. To make $T \to 1$, we have

$$(\epsilon_{a1} + \epsilon_{a2}e^{-i2m_a\beta_{a2}})\epsilon_b e^{-i2m_b\beta_b}e^{2i\theta} = -\gamma_{1,1}\gamma_{1,2}/4,$$
 (S21)

$$\left(\epsilon_{a1} + \epsilon_{a2}e^{i2m_b\beta_{a2}}\right) = 0, (S22)$$

where Eq. (S21) is a specific form of Eq. (S17), and Eq. (S22) describes the condition for EP₊. By choosing $\beta_b = 0$, we have

$$\epsilon_{a2} \sin(2m_a \beta_{a2}) \epsilon_b e^{i(2\theta + \frac{\pi}{2})} = \gamma_{1,1} \gamma_{1,2} / 8.$$
 (S23)

This condition is hard to be achieved by experimental parameters.

A4. Standing wave approximation for μR_2

In some cases, μR_2 can be regarded as a standing wave (SW) resonator, which will simplify the calculation and be able to give rise to more prominent EPAT effect. We now offer the analysis of how this approximation will be valid. Generically, the loss of μR_2 is composed of the intrinsic loss of the resonator (including material absorption and radiation loss) and the scattering loss induced by the Raleigh scatters on the surface of the resonator. The eigenvalues of the two supermodes in μR_2 are given by $\omega_2 - i\gamma_{0,2}/2$ and $\omega_2 - i\gamma_{0,2}/2 + 2\epsilon_b$, respectively. If the scattering loss plays a dominant role in the total loss, which corresponds to the condition that $2Im(\epsilon_a) \gg \gamma_{0,1}$, then the two supermodes will have vastly different loss rates, $\gamma_{0,2}/2$ and $\gamma_{0,2}/2 - 2Im(\epsilon_b)$, respectively. Therefore, under the same coupling strength, the two modes may be under different coupling regimes. For example, the less lossy one is critically coupled to the taper, and the lossy one is undercoupled to the taper. Under this case, if the real part of ϵ_b is much smaller than the imaginary part, the supermodes also have a large overlap in the transmission spectrum. As a result, only the less lossy supermode is observable, and plays a dominant role

when interacting with the modes in μR_1 indirectly through the taper. Therefore, we can neglect the lossy supermode directly from the very beginning. The model will be composed of a chirality-broken WGM resonator coupled indirectly to a SW cavity. This approximation not only reveals the possibility of having single SW mode structure in WGM cavities, but also enables the system to mimic the coupling between Fabry-Perot cavities which support SW modes. This model opens up the potential scenario of fundamental studies and applications in WGM resonators and the coupling systems.

We now offer a rigid proof of the equivalence between the direct treatment of μR_2 as a SW cavity and the approximation that scattering loss is large.

By treating μR_2 as a SW cavity, the coupled mode equations become

$$\frac{da_1}{dt} = -i\omega_1 a_1 - \frac{\gamma_{0,1} + \gamma_{1,1}}{2} a_1 - i\kappa_{a21} a_2 - \sqrt{\gamma_{1,1}} a_{in}, \tag{S24}$$

$$\frac{da_2}{dt} = -i\omega_1 a_2 - \frac{\gamma_{0,1} + \gamma_{1,1}}{2} a_2 - i\kappa_{a12} a_1 - e^{i\theta} \sqrt{\gamma_{1,1} \gamma_{1,2}} b,$$
 (S25)

$$\frac{db}{dt} = -i\omega_2 b - \frac{\gamma_{0,2} + 2\gamma_{1,2}}{2} b - e^{i\theta} \sqrt{\gamma_{1,1}\gamma_{1,2}} a_1 - e^{i\theta} \sqrt{\gamma_{1,2}} a_{in}.$$
 (S26)

In the frequency domain,

$$0 = \left(i\Delta_1 - \frac{\gamma_{0,1} + \gamma_{1,1}}{2}\right) a_1[\omega] - i\kappa_{a21} a_2[\omega] - \sqrt{\gamma_{1,1}} a_{in}[\omega], \tag{S27}$$

$$0 = \left(i\Delta_1 - \frac{\gamma_{0,1} + \gamma_{1,1}}{2}\right)a_2[\omega] - i\kappa_{a_{12}}a_1[\omega] - e^{i\theta}\sqrt{\gamma_{1,1}\gamma_{1,2}}b[\omega],\tag{S28}$$

$$0 = \left(i\Delta_2 - \frac{\gamma_{0,2} + 2\gamma_{1,2}}{2}\right)b[\omega] - e^{i\theta}\sqrt{\gamma_{1,1}\gamma_{1,2}}a_1[\omega] - e^{i\theta}\sqrt{\gamma_{1,2}}a_{in}[\omega],\tag{S29}$$

where $\Delta_1 = \omega - \omega_1$ and $\Delta_2 = \omega - \omega_2$. The output is given by:

$$a_{out} = e^{i\theta} (a_{in} + \sqrt{\gamma_{1,1}} a_1) + \sqrt{\gamma_{1,2}} b.$$
 (S30)

From here, when $\Delta = \Delta_1 = \Delta_2$, we can obtain the transmission as

$$T = \left| \left(i\Delta - \frac{\gamma_{0,2}}{2} \right) - \frac{\left(i\Delta - \frac{\gamma_{0,1}}{2} \right)^2 - \left(\frac{\gamma_{1,1}}{2} \right)^2 + \kappa_{a21} \kappa_{a12}}{-i\gamma_{1,1}\gamma_{1,2}\kappa_{a21}e^{2i\theta} + \left[\left(i\Delta - \frac{\gamma_{0,1} + \gamma_{1,1}}{2} \right)^2 + \kappa_{a21}\kappa_{a12} \right] \left(i\Delta - \frac{\gamma_{0,2} + 2\gamma_{1,2}}{2} \right) \right|^2.$$
 (S31)

On the other hand, we start from the general model we provided in Section A1. The transmission spectrum under the condition $|Im(\epsilon_b)| \gg \gamma_{0,2}$, $|Re(\epsilon_b)|$ is given by

$$T \approx \left| \frac{\left(\left(i\Delta - \frac{\gamma'_{0,1}}{2} \right)^2 - \left(\frac{\gamma_{1,1}}{2} \right)^2 + \kappa_{a21}\kappa_{a12} \right) \left(\left(i\Delta - \frac{\gamma'_{0,2}}{2} \right)^2 - \left(\frac{\gamma_{1,2}}{2} \right)^2 - \left(\frac{\gamma'_{0,2}}{2} \right)^2 \right)}{\gamma_{1,1}\gamma_{1,2}\kappa_{a21}\epsilon_b e^{2i\theta} + \left(\left(i\Delta - \frac{\gamma'_{0,1} + \gamma_{1,1}}{2} \right)^2 + \kappa_{a21}\kappa_{a12} \right) \left(i\Delta - \frac{\gamma'_{0,2} + 2\gamma_{1,2}}{2} \right) \left(i\Delta - \frac{\gamma'_{0,2}}{2} \right)^2} \right|^2.$$
 (S32)

Now by comparison of the results from two models, we can see that when Δ is small, the transmission spectra described by Eq. (S31) and Eq. (S32) are the same, and thus the SW treatment of μR_2 is valid in our study of the EPAT and EPAA.

Furthermore, if $\Delta = 0$,

$$T = \left| \frac{\gamma_{1,2} \left(-\left(\gamma_{0,1} - 2Im(\epsilon_{a1} + \epsilon_{a2})\right)^2 + \gamma_{1,1}^2 - 4\kappa_{a21}\kappa_{a12}\right)}{16\gamma_{1,1}\kappa_{a21}\epsilon_b e^{2i\theta} + \left(4\epsilon_b'' + \gamma_{1,2}\right) \left(\left(\gamma_{0,1} + \gamma_{1,1} - 2Im(\epsilon_{a1} + \epsilon_{a2})\right)^2 + 4\kappa_{a21}\kappa_{a12}\right) \right|^2} \right|. \tag{S33}$$

Thus, under SW approximation for μR_2 , we can study the trend of the peak of EIT or EPAT using Eq. (S33).

B. Effect of polarization

In our theoretical and experimental study, we found that the mismatch of polarizations in the two resonators could significantly modify the transmission spectrum. Here we offer an analysis of the system given that the polarizations in two resonators do not align with each other.

We choose the polarization of modes in μR_2 in the x direction, and the polarization of modes in μR_1 to have an angle ϕ with respect to the x direction. If the incident light has a polarization in the x direction, the coupled mode equations are modified as⁸:

$$\frac{d}{dt} \binom{a_1}{a_2} = \begin{pmatrix} -i\omega_1 - \frac{\gamma_{0,1} + \gamma_{1,1}}{2} & -i\kappa_{a21} \\ -i\kappa_{a12} & -i\omega_1 - \frac{\gamma_{0,1} + \gamma_{1,1}}{2} \end{pmatrix} \binom{a_1}{a_2} - \sqrt{\gamma_{1,1}} \cos(\phi) \binom{a_{in}}{e^{i\theta} b'_{outx}}, \quad (S34)$$

$$\begin{pmatrix} a'_{outx} \\ b_{outx} \end{pmatrix} - \begin{pmatrix} a_{in} \\ e^{i\theta} b'_{outx} \end{pmatrix} = \sqrt{\gamma_{1,1}} \cos(\phi) \begin{pmatrix} a_1 \\ a_2 \end{pmatrix},$$
 (S35)

$$\begin{pmatrix} a'_{outy} \\ b_{outy} \end{pmatrix} - \begin{pmatrix} 0 \\ 0 \end{pmatrix} = \sqrt{\gamma_{1,1}} \sin(\phi) \begin{pmatrix} a_1 \\ a_2 \end{pmatrix},$$
 (S36)

$$\frac{d}{dt} \binom{b_1}{b_2} = \begin{pmatrix} -i\omega_2 - \frac{\gamma_{0,2} + \gamma_{1,2}}{2} & -i\kappa_{b21} \\ -i\kappa_{b12} & -i\omega_2 - \frac{\gamma_{0,2} + \gamma_{1,2}}{2} \end{pmatrix} \binom{b_1}{b_2} - \sqrt{\gamma_{1,2}} \binom{e^{i\theta} a'_{outx}}{0}, \tag{S37}$$

$$\binom{a_{outx}}{b'_{outx}} - \binom{e^{i\theta}a'_{outx}}{0} = \sqrt{\gamma_{1,2}} \binom{b_1}{b_2},$$
 (S38)

$$\binom{a_{outy}}{b'_{outy}} - \binom{e^{i\theta}a'_{outy}}{0} = 0,$$
 (S39)

where a_{outx} , a_{outy} , a'_{outx} , a'_{outy} , b_{outx} , b_{outy} , b'_{outx} and b'_{outy} are x and y components of a_{out} , a'_{out} , b_{out} and b'_{out} , respectively. By numerically solving Eqs. (S34)-(S39) in frequency domain, we can obtain the values of a_{outx} and a_{outy} and calculate the transmission by

$$T = |t_x|^2 + |t_y|^2 = |a_{outx}/a_{in}|^2 + |a_{outy}/a_{in}|^2.$$
 (S40)

In our study of EPAA and EPAT, the polarization mismatch ϕ is minimized as small as 0.03π to avoid significant influence on the transmission signal. When the polarization mismatch is large, the spectrum can exhibit a high peak within a broad absorption dip even without any interference effect. This kind of polarization effect is different from EIT^{9–22}, OMIT^{23–27}, Brillouin scattering induced transparency (BSIT)^{28,29} or EPAT which are based on classical or quantum interference^{30–32} and have led to slow light^{12,33–42}. But the sharp peak in the spectrum may also be used for sensing applications^{9,43}.

Theoretically, we could also obtain EPAA and EPAT without polarization mismatch. The dependence of splitting type of EIT, EPAA and EPAT on the phase angle θ is shown in Fig. S3. As predicted in the main text, EPAA is invariant with θ , whereas EIT and EPAT change periodically with θ .

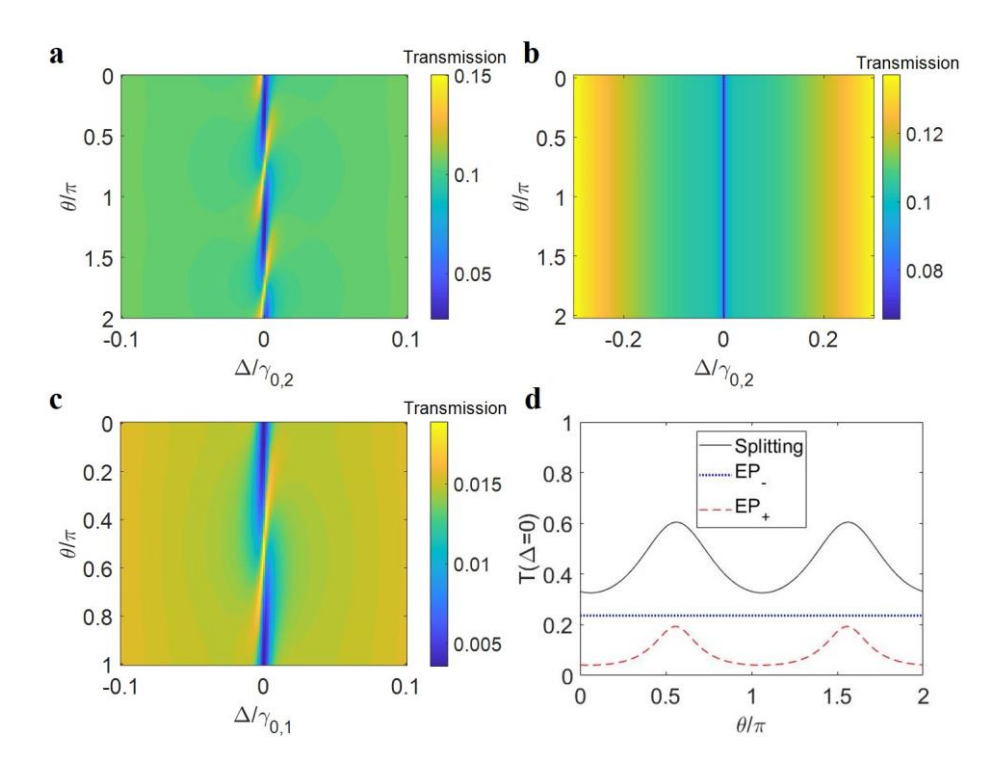


Fig. S3 | Theoretical study of interference effect with perfect polarization match between resonators. a-c, Simulation result of the transmission spectrum in splitting case (a), EP₋ case (b) and EP₊ case (c). d, Transmission signal at zero detuning point ($\Delta = 0$) vs. phase angle θ .

C. Extended experimental and simulation results

C1. EIT and EIA with splitting

As mentioned in Section A1, we not only studied the case of EP₊ and EP₊, but also the case when μR_1 has unbroken chiral symmetry without external perturbation to the microtoroid μR_1 . We align the resonant frequencies of μR_2 to that of μR_1 by tuning the temperature of μR_2 via the TEC⁴⁴. $\gamma_{1,2}$ is tuned by adjusting the gap between μR_2 and the taper to make μR_2 weakly coupled to the taper. When

the coupling between μR_1 and the fibre taper is weak $(\gamma_{1,1} \ll \gamma_{0,1})$, the transmission spectrum exhibits a broad dip (from μR_2) overlapping with a narrow dip (from μR_1) at the zero detuning (Fig. S4a). By increasing $\gamma_{1,1}$, i.e., moving μR_1 close to the fibre taper, the narrow dip in the transmission spectrum goes upwards, gradually disappears, and then is turned into a narrow peak out of a wide absorption dip, similar to an EIT lineshape (Fig. S4b). Here in both absorption and transparency windows, the mode splitting is observed, indicating that each supermode in μR_1 couples with the supermodes in μR_2 . The splitting in the broad dip is indistinguishable due to the large linewidths. Therefore, we verified that the interactions between four supermodes corresponding to the levels $\omega_{1,\pm}$ and $\omega_{2,\pm}$ could result in the splitting type of EIT. Moreover, in the above two mentioned cases shown in Figs. S4a and S4b, the phase θ was chosen by adjusting the distance between resonators so that the destructive interference occurs in the output waveguide channel, judged by observing the shallowest dip and the highest peak, respectively. When we fix μR_1 to be close to the waveguide and tune θ periodically via adjusting the distance between the resonators, the interference varies between destructive and constructive periodically. This is clearly shown by observing the periodic alternation between absorption and transparency when the distance is changed under the condition that $\gamma_{1,1}$ is large (Fig. S4c). This periodic appearance of splitting types of EIT and EIA is also found theoretically by changing θ with a period of 2π (Fig. S4d). To match the experimental result, a polarization mismatch of 0.08π is introduced in the theoretical model. We note that when the polarization mismatch is large, EIT-like transmission spectrum could appear even without any loop interference, which has been discussed before. Similar to the conventional system with EIT, the transparency peaks observed here will evolve into Fano resonances when there is a deviation between the resonant frequencies of μR_1 and μR_2 . Additionally, under the weak coupling condition $(\gamma_{1,1} \ll \gamma_{0,1})$, dips do not turn into peaks but their depths also vary periodically with phase change.

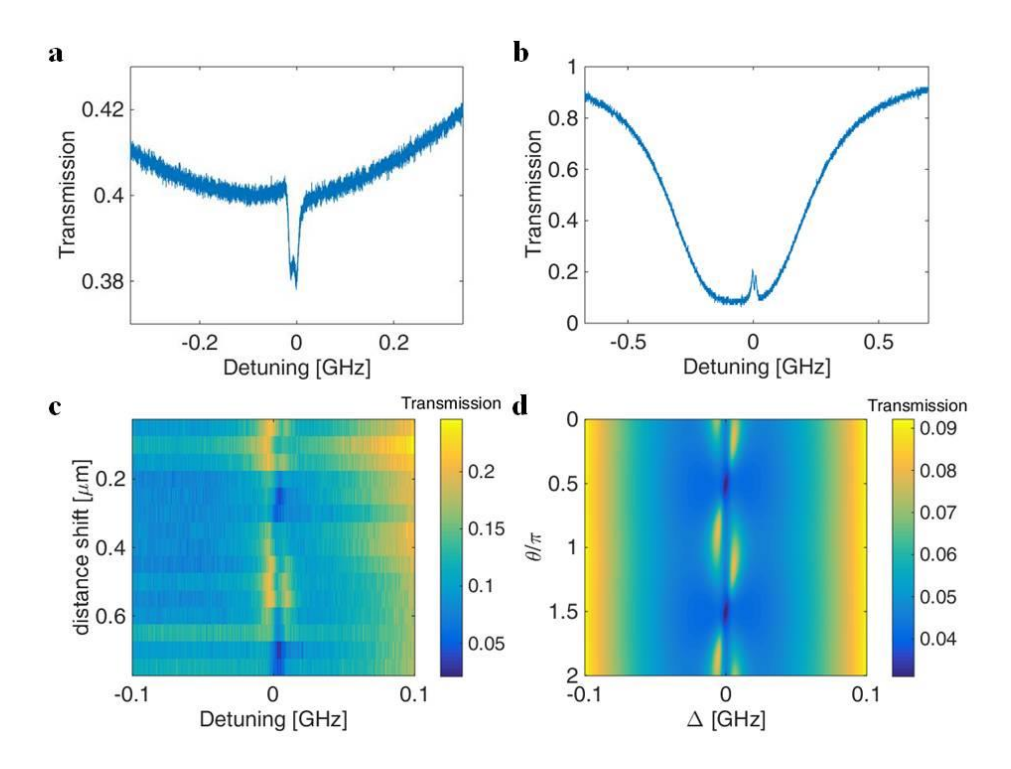


Fig. S4 | Transmission spectra for indirectly coupled resonators without nanotip. a, Transmission spectrum when the coupling between μR_1 and the taper is weak. b, Transmission spectrum when the

coupling between μR_1 and the taper is strong. **c**, Experimentally obtained evolution of transmission spectra with variation of the distance between the two resonators. From top to bottom the distance is changed by a step of 50 nm. **d**, Theoretical result of the evolution of transmission spectra with different values of phase shift θ . Parameters: $\gamma_{0,1} = 2.992 \text{MHz}$, $\gamma_{0,2} = 0.1316 \text{ GHz}$, $\gamma_{1,1} = 5.984 \text{ MHz}$, $\gamma_{1,2} = 0.4343 \text{ GHz}$, $\kappa_{a21} = \kappa_{a12} = (3.565 - 0.0159i) \text{ MHz}$, $\kappa_{b21} = \kappa_{b12} = (0.1337 - 0.0306i) \text{ GHz}$, polarization mismatch $\phi = 0.08\pi$.

C2. Effect of frequency detuning between two resonators

Similar to the conventional EIT, the interference in indirectly coupled resonators could also induce Fano resonance^{3,8,18,45}. Fano resonance occurs when a discrete state interferes with a continuum. It has been proposed for many useful applications including slow light and sensing. Here when the resonances of μR_1 lie within the range of the wide spectrum of μR_2 , the sharp high-Q state is coupled to the low-Q state with a broad linewidth which could be regarded as a continuum state, thus yielding Fano resonance. In the main text and Section C1 of Supplementary Information, Fano lineshapes have already been observed in the study of EPAT and the splitting type of EIT, when the phase θ is not optimized for destructive or constructive interference. Here we found in experiment that the Fano resonance could also appear when the frequency detuning between μR_1 and μR_2 is nonzero (Fig. S5). The parameters, such as coupling strengths and backscattering rates, are similar to those in the study of EPAT and the splitting type of EIT.

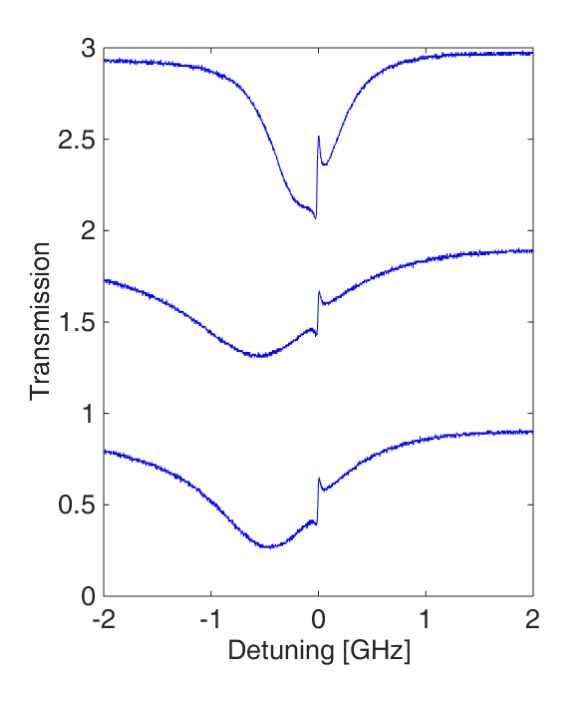


Fig. S5 | Experimental results of Fano resonance. From top to bottom the coupling between μR_2 and the taper is increased, which also results in a red shift of the broad absorption dip.

C3. Effect of coupling strengths between the resonators and the fibre taper

Within the parameter range in our experiment, the larger coupling strengths between the resonators and the taper are favorable for the interference effect. As shown in Fig. S6a, when the coupling strength between μR_1 and the taper is weak, EIT has a very small peak. By decreasing the gap between μR_1 and the taper, $\gamma_{1,1}$ becomes larger, which leads to a higher peak in the EIT lineshape. Furthermore, $\gamma_{1,2}$ has a similar effect on interference (Fig. S6b). Initially when $\gamma_{1,2}$ is small, transmission spectrum shows the narrow resonance of the high-Q mode in μR_1 , as well as two broad dips corresponding to the widely splitting supermodes in μR_2 . We align the frequencies of the high-Q resonance with one of the low-Q resonance so that the narrow dip overlaps with one of the broad dips in the spectrum. Initially when $\gamma_{1,2}$ is small, transmission spectra show absorption with no signature of interference. When $\gamma_{1,2}$ increases, the two broad dips are dragged downwards and gradually merge into one, while the interference effects (Fano resonance) become observable. Here the red shift of the broad dips becomes increasingly obvious with stronger coupling, due to the larger resonance scattering induced by the taper⁴⁶.

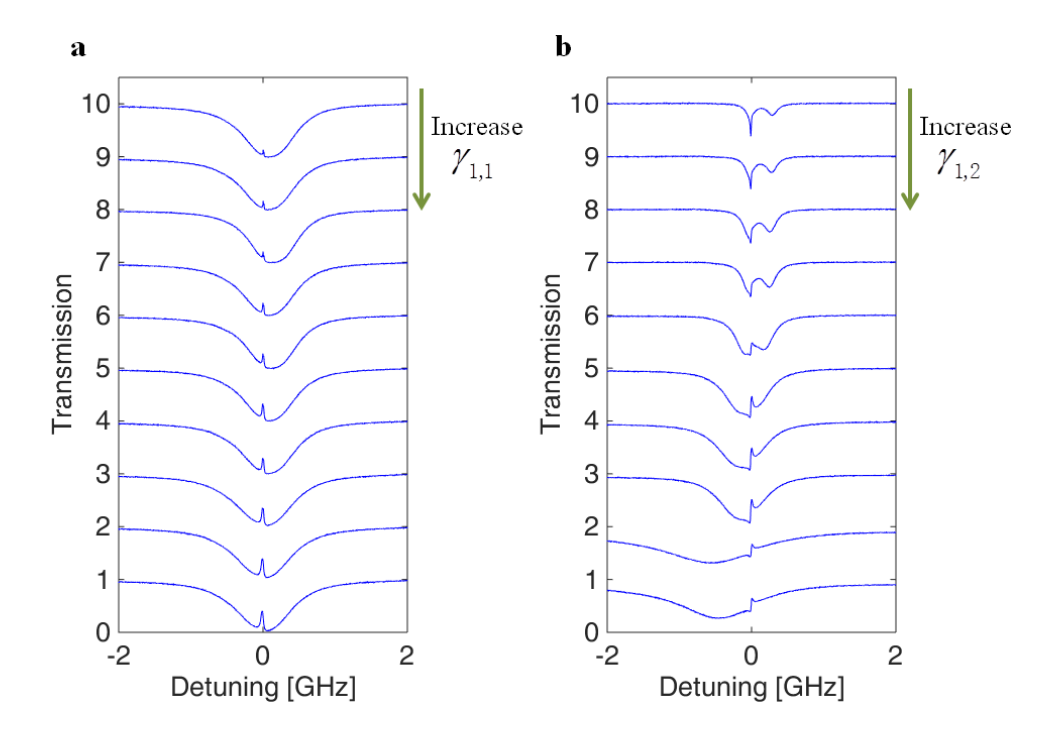


Fig. S6 | Experimental results of the effect of coupling strengths between resonators and the taper. a, Transmission spectra with different coupling strengths $\gamma_{1,1}$. From top to bottom the gap between μR_1 and the taper is decreased by as step of 50nm, corresponding to increasing $\gamma_{1,1}$. b, Transmission spectra with different coupling strengths $\gamma_{1,2}$. From top to bottom the gap between μR_1 and the taper is decreased by as step of 50 nm, corresponding to increasing $\gamma_{1,2}$.

We also numerically study the influence of $\gamma_{1,1}$ on EPAT, as shown in Fig. S7. The corresponding experimental results are shown in Fig. 4c of the main text.

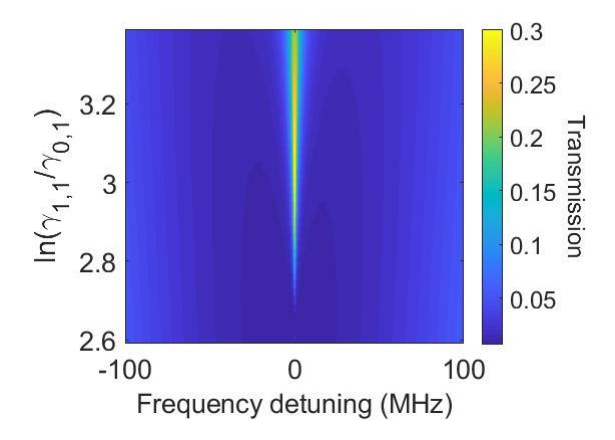


Fig. S7 | Numerical study of the effect of the coupling strength $\gamma_{1,1}$. Parameters: $\kappa_{a21}=(92.77-32.12\mathrm{i})$ MHz , $\kappa_{a12}=0$, $\kappa_{b21}=\kappa_{b12}=(0.1337-0.0306\mathrm{i})$ GHz , $\theta=0.6\pi$, $\gamma_{0,1}=3.024$ MHz , polarization mismatch $\phi=0.03\pi$.

C4. Tuning between chiral states

The tuning between the two chiral states (1 and -1) of μR_1 in our system can be achieved by adjusting the azimuthal position of the nanotip to change the relative phase angle ($\beta_{a2} - \beta_{a1}$). The relation between chirality and relative phase angle has been experimentally shown by Peng et al⁴⁷. Here we numerically show the relation between chirality and the phase angle β_{a2} (with fixed β_{a1}) in Fig. S8. Note that this kind of chirality tuning is different from the asymmetric mode switching when dynamically encircling an EP⁴⁸⁻⁵⁰.

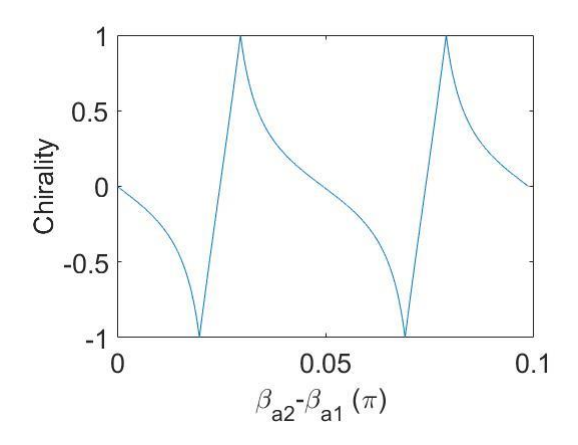


Fig. S8 | Numerical study of the relation between chirality and the relative phase angle $(\beta_{a2} - \beta_{a1})$. Parameters: azimuthal mode number m = 200, $\epsilon_{a1} = (3.557 - 0.01210i)$ MHz, $\epsilon_{a2} = (2.865 - 2.101i)$ MHz.

References

1. Yariv, A. Coupled-Mode Theory for Guided-Wave Optics. *IEEE J. Quantum Electron.* **9**, 919–933 (1973).

- 2. Yanik, M. F., Suh, W., Wang, Z. & Fan, S. Stopping Light in a Waveguide with an All-Optical Analog of Electromagnetically Induced Transparency. *Phys. Rev. Lett.* **93**, 233903 (2004).
- 3. Xiao, Y.-F. *et al.* Asymmetric Fano resonance analysis in indirectly coupled microresonators. *Phys. Rev. A* **82**, 065804 (2010).
- 4. Xiao, Y. F., Zou, X. B., Jiang, W., Chen, Y. L. & Guo, G. C. Analog to multiple electromagnetically induced transparency in all-optical drop-filter systems. *Phys. Rev. A* **75**, 063811 (2007).
- 5. Zhu, J., Özdemir, Ş. K., He, L. & Yang, L. Controlled manipulation of mode splitting in an optical microcavity by two Rayleigh scatterers. *Opt. Express* **18**, 23535–23543 (2010).
- 6. Shao, L. *et al.* Detection of Single Nanoparticles and Lentiviruses Using Microcavity Resonance Broadening. *Adv. Mater.* **25**, 5616–5620 (2013).
- 7. Jiang, X. *et al.* Chaos-assisted broadband momentum transformation in optical microresonators. *Science* **358**, 344–347 (2017).
- 8. Li, B.-B. *et al.* Experimental observation of Fano resonance in a single whispering-gallery microresonator. *Appl. Phys. Lett.* **98**, 021116 (2011).
- 9. Zhao, G. *et al.* Raman lasing and Fano lineshapes in a packaged fiber-coupled whispering-gallery-mode microresonator. *Sci. Bull.* **62**, 875–878 (2017).
- 10. Dong, C.-H. *et al.* Modified transmission spectrum induced by two-mode interference in a single silica microsphere. *J. Phys. B At. Mol. Opt. Phys.* **42**, 215401 (2009).
- 11. Dmochowski, G. *et al.* Experimental Demonstration of the Effectiveness of Electromagnetically Induced Transparency for Enhancing Cross-Phase Modulation in the Short-Pulse Regime. *Phys. Rev. Lett.* **116**, 173002 (2016).
- 12. Albert, M., Dantan, A. & Drewsen, M. Cavity electromagnetically induced transparency and all-optical switching using ion Coulomb crystals. *Nat. Photonics* **5**, 633–636 (2011).
- 13. Zhu, S. *et al.* All-optical controllable electromagnetically induced transparency in coupled silica microbottle cavities. *Nanophotonics* **7**, 1669–1677 (2018).
- 14. Xiao, Y. F., He, L., Zhu, J. & Yang, L. Electromagnetically induced transparency-like effect in a single polydimethylsiloxane-coated silica microtoroid. *Appl. Phys. Lett.* **94**, 231115 (2009).
- 15. Yang, Y., Saurabh, S., Ward, J. & Chormaic, S. N. Coupled-mode-induced transparency in aerostatically tuned microbubble whispering-gallery resonators. *Opt. Lett.* **40**, 1834–1837 (2015).
- 16. Yang, X., Yu, M., Kwong, D. L. & Wong, C. W. All-optical analog to electromagnetically induced transparency in multiple coupled photonic crystal cavities. *Phys. Rev. Lett.* **102**, 173902 (2009).
- 17. Zheng, Y. et al. Optically induced transparency in a micro-cavity. Light Sci. Appl. 5, e16072 (2016).
- 18. Li, B.-B. *et al.* Experimental controlling of Fano resonance in indirectly coupled whispering-gallery microresonators. *Appl. Phys. Lett.* **100**, 021108 (2012).
- 19. Naweed, A., Farca, G., Shopova, S. I. & Rosenberger, A. T. Induced transparency and absorption in coupled whispering-gallery microresonators. *Phys. Rev. A* **71**, 043804 (2005).
- 20. Chen, W., Beck, K. M., Bücker, R., Gullans, M., Lukin, M. D., Tanji-Suzuki, H., & Vuletić, V. All-Optical Switch and Transistor Gated by One Stored Photon. *Science* **341**, 768–770 (2013).
- 21. Harris, S. E. & Yamamoto, Y. Photon switching by quantum interference. *Phys. Rev. Lett.* **81**, 3611–3614 (1998).
- 22. Schmidt, H. & Imamoglu, A. Giant Kerr nonlinearities obtained by electromagnetically induced

- transparency. Opt. Lett. 21, 1936–1938 (1996).
- 23. Dong, C., Fiore, V., Kuzyk, M. C., & Wang, H. Optomechanical Dark Mode. *Science* **338**, 1606–1609 (2012).
- 24. Jing, H. *et al.* Optomechanically-induced transparency in parity-time-symmetric microresonators. *Sci. Rep.* **5**, 9663 (2015).
- 25. Liu, Y.-L. *et al.* Controllable optical response by modifying the gain and loss of a mechanical resonator and cavity mode in an optomechanical system. *Phys. Rev. A* **95**, 13843 (2017).
- 26. Wang, B., Liu, Z.-X., Kong, C., Xiong, H. & Wu, Y. Mechanical exceptional-point-induced transparency and slow light. *Opt. Express* **27**, 8069–8080 (2019).
- 27. Shen, Z. *et al.* Experimental realization of optomechanically induced non-reciprocity. *Nat. Photonics* **10**, 657–661 (2016).
- 28. Kim, J., Kuzyk, M. C., Han, K., Wang, H. & Bahl, G. Non-reciprocal Brillouin scattering induced transparency. *Nat. Phys.* **11**, 275–280 (2015).
- 29. Dong, C.-H. *et al.* Brillouin-scattering-induced transparency and non-reciprocal light storage. *Nat. Commun.* **6**, 6193 (2015).
- 30. Wang, C., Liu, Y. L., Wu, R. & Liu, Y. X. Phase-modulated photon antibunching in a two-level system coupled to two cavities. *Phys. Rev. A* **96**, 13818 (2017).
- 31. Zhao, Y. J., Wang, C., Zhu, X. & Liu, Y. X. Engineering entangled microwave photon states through multiphoton interactions between two cavity fields and a superconducting qubit. *Sci. Rep.* **6**, 23646 (2016).
- 32. Liu, Y. L., Wang, G. Z., Liu, Y. X. & Nori, F. Mode coupling and photon antibunching in a bimodal cavity containing a dipole quantum emitter. *Phys. Rev. A* **93**, 013856 (2016).
- 33. Lvovsky, A. I., Sanders, B. C. & Tittel, W. Optical quantum memory. *Nat. Photonics* **3**, 706–714 (2009).
- 34. Totsuka, K., Kobayashi, N. & Tomita, M. Slow Light in Coupled-Resonator-Induced Transparency. *Phys. Rev. Lett.* **98**, 213904 (2007).
- 35. Matsukevich, D. N. *et al.* Storage and retrieval of single photons transmitted between remote quantum memories. *Nature* **438**, 833–836 (2005).
- 36. Wang, Y. *et al.* Efficient quantum memory for single-photon polarization qubits. *Nat. Photonics* **13**, 346–351 (2019).
- 37. Marx, A. *et al.* Slowing, advancing and switching of microwave signals using circuit nanoelectromechanics. *Nat. Phys.* **9**, 179–184 (2013).
- 38. Lukin, M. D. & Imamoğlu, A. Controlling photons using electromagnetically induced transparency. *Nature* **413**, 273–276 (2001).
- 39. Vestergaard Hau, L., Harris, S. E., Dutton, Z. & Behroozi, C. H. Light speed reduction to 17 metres per second in an ultracold atomic gas. *Nature* **397**, 594–598 (1999).
- 40. Wu, B. et al. Slow light on a chip via atomic quantum state control. Nat. Photonics 4, 776–779 (2010).
- 41. Liu, C., Dutton, Z., Behroozi, C. H., & Hau, L. V. Observation of coherent optical information storage in an atomic medium using halted light pulses. *Nature* **409**, 490–493 (2001).
- 42. Phillips, D. F., Fleischhauer, A., Mair, A., Walsworth, R. L. & Lukin, M. D. Storage of light in atomic vapor. *Phys. Rev. Lett.* **86**, 783–786 (2001).

- 43. Zhu, J., Zhao, G., Savukov, I. & Yang, L. Polymer encapsulated microcavity optomechanical magnetometer. *Sci. Rep.* **7**, 8896 (2017).
- 44. Jiang, X. & Yang, L. Opto-thermal dynamics in whispering-gallery microresonators. arXiv:1911.06789 (2019).
- 45. Shang, Y.-L., Ye, M.-Y. & Lin, X.-M. Experimental observation of Fano-like resonance in a whispering-gallery-mode microresonator in aqueous environment. *Photonics Res.* **5**, 119–123 (2017).
- 46. Jiang, X.-F. *et al.* Highly unidirectional emission and ultralow-threshold lasing from on-chip ultrahigh-Q microcavities. *Adv. Mater.* **24**, 260–264 (2012).
- 47. Peng, B. *et al.* Chiral modes and directional lasing at exceptional points. *Proc. Natl. Acad. Sci.* **113**, 6845–6850 (2016).
- 48. Hassan, A. U., Zhen, B., Soljačić, M., Khajavikhan, M. & Christodoulides, D. N. Dynamically Encircling Exceptional Points: Exact Evolution and Polarization State Conversion. *Phys. Rev. Lett.* **118**, 093002 (2017).
- 49. Zhang, X.-L., Wang, S., Hou, B. & Chan, C. T. Dynamically Encircling Exceptional Points: In situ Control of Encircling Loops and the Role of the Starting Point. *Phys. Rev. X* **8**, 021066 (2018).
- 50. Doppler, J. *et al.* Dynamically encircling an exceptional point for asymmetric mode switching. *Nature* **537**, 76–79 (2016).